Breakup reactions of ^{11}Li within a three-body model

E. Garrido
Instituto de Estructura de la Materia, CSIC, Serrano 123, E-28006 Madrid, Spain

D. V. Fedorov and A. S. Jensen
Institute of Physics and Astronomy, Aarhus University, DK-8000 Aarhus C, Denmark
(Received 5 November 1998)

We use a three-body model to investigate breakup reactions of ^{11}Li $(n+n+^{9}\mathrm{Li})$ on a light target. The interaction parameters are constrained by known properties of the two-body subsystems, the ^{11}Li binding energy and fragmentation data. The remaining degrees of freedom are discussed. The projectile-target interactions are described by phenomenological optical potentials. The model predicts dependence on beam energy and target, differences between longitudinal and transverse momentum distributions, and provides absolute values for all computed differential cross sections. We give an almost complete series of observables and compare with corresponding measurements. Remarkably good agreement is obtained. The relative neutron-^{9}Li p-wave content is about 40%. A p-resonance, consistent with measurements at about 0.5 MeV of width about 0.4 MeV, seems to be necessary. The widths of the momentum distributions are insensitive to target and beam energy with a tendency to increase towards lower energies. The transverse momentum distributions are broader than the longitudinal ones due to the diffraction process. The absolute values of the cross sections follow the neutron-target cross sections and increase strongly for beam energies decreasing below 100 MeV/nucleon. [S0556-2813(99)02103-2]

PACS number(s): 25.60.Gc, 21.60.Gx, 21.45.+v

I. INTRODUCTION

Large efforts are devoted to investigate the properties of halo nuclei [1,2]. In particular two-neutron halo nuclei have attracted a lot of attention with ^{6}He $(n+n+^{4}\mathrm{He})$ and ^{11}Li $(n+n+^{9}\mathrm{Li})$ as the most prominent examples. These nuclei are also Borromean three-body systems, where all two-body subsystems are unbound [3,4]. The two neutrons (the halo) are weakly bound to an ordinary nucleus (the core). The halo is spatially extended and the two neutrons have a high probability of being outside the core. The core and halo degrees of freedom then approximately decouple and three-body models provide a good description of such systems.

The most detailed properties of halo nuclei are obtained by measurements of fragment momentum distributions in breakup reactions on stable targets [5–17]. The projectile energy in these reactions is very large compared to the energies of the intrinsic motion of the nucleons in the core, which in turn is much larger than the binding energies of the spatially extended halo particles. Such high-energy reactions are tempting to describe in the sudden approximation where the three-body binding is removed without disturbing the motion of the constituent particles. The three halo particles continue their motion independently without any further interaction. The resulting momentum distributions then reflect the motion in the initial halo bound state of the two neutrons and the core. Thus the unchanged initial three-body wave function should describe the observed momentum distributions. The Fourier transform of the wave function indeed approximately reproduces the core momentum distribution [3,18–22]. However, the calculated neutron distributions are significantly broader than measured.

Improvements using Glauber theory are possible [23,24], but the neutron distributions within this approach are only reported for two-neutron halos in [24], where the two-neutron removal cross sections and the related momentum distributions are nicely described. However, an alternative is to improve the physically intuitive geometric picture established by the successful sudden approximation. The next step in such a description then amounts to instantaneous removal of one halo particle (participant) while the remaining two particles (spectators) continue to interact on the way to detection. This modification has only little influence on the core momentum distribution but affects significantly the distribution of the lighter neutron. Several authors suggested that this final state interaction between the spectators plays an essential role, especially when low-lying resonances are present [10,19,25]. Indeed computations then reproduce the measured momentum distributions remarkably well when the final state interaction in a consistent calculation is precisely the same as in the initial three-body wave function [21,22]. In addition the model also fairly well describes the invariant mass spectra for the two-body system consisting of the core and the remaining neutron.

This successful model requires, however, a better justification. The sudden approximation assumes that the transition amplitude is proportional to the overlap between initial and final state wave functions and the momentum distributions are simply proportional to the square of this overlap. The participant-target interactions, implicitly used, are described as the schematic black sphere scattering where only absorption is considered. The obvious improvement is to use the phenomenological optical model to describe the interaction between the participant and the target [26,27]. The qualitative improvement is then inclusion of elastic scattering in addition to absorption.

At the high energies, where these models mostly are

tested, neutron elastic scattering is about three times smaller than neutron absorption [28]. However, the neutron momentum distribution is much broader for elastic scattering than for absorption. The contribution from neutron scattering is therefore important. Whether the predictions would agree with measurements still remains to be studied systematically. The first important step is to assume that the optical model describes the interaction between the target and the participant whereas the spectators remain undisturbed by the target but still continue their motion under the influence of their mutual interaction. The complete three-body breakup reaction is then described as a sum of these three independent contributions. We then neglect processes where two or three halo particles interact simultaneously with the target [26,27].

The three-body model is strictly only valid for structureless particles. The effects of extended density distributions for the constituent particles are small when the major part of the three-body wave function is outside the radii of all the three particles. However, this requirement is usually not completely satisfied for halo nuclei. The model is then only accurate for the outer part of the wave function. Furthermore, the spatial extensions of the particles and the target allow geometric configurations where more than one halo particle during the collision must get close to the target. These configurations should be excluded in the process. For one-nucleon halos this so-called shadowing effect is known to produce smaller absolute cross sections and narrower momentum distributions [29–31]. For two-neutron halos the shadowing effect was included through profile functions in sophisticated Glauber calculations of three-body fragmentation reactions [24]. We account for shadowing by excluding the participant wave function inside spheres around the two spectators [26,27].

The model then consists of an initial three-body halo state, reactions caused by the participant-target optical potential, a final state with two independent two-body systems, i.e., the two spectators and the participant-target, and shadowing which excludes the wave function within spheres around the spectators. The differential cross sections are then products of the participant-target cross section and the square of the overlap previously used in the pure sudden approximation. The results from the successful sudden approximation are essentially recovered, but the model now also, via the optical potential, contains dependence on beam energy and target, distinction between longitudinal and transverse momenta and also absolute values of all the cross sections.

The purpose of this paper is to investigate the breakup reactions of ^{11}Li within the three-body model sketched above. We shall show systematic computations of a number of observables and predict or compare with measurements. The results are then all correlated as arising from the same model with one set of parameters. In Sec. II we descibe the model and the method. In Sec. III we compare our results with the available experimental information and select an interaction with corresponding shadowing parameters which best fits the experimental data. Section IV presents predictions for a number of observables including their energy dependence. Finally Sec. V contains a summary and the conclusions.

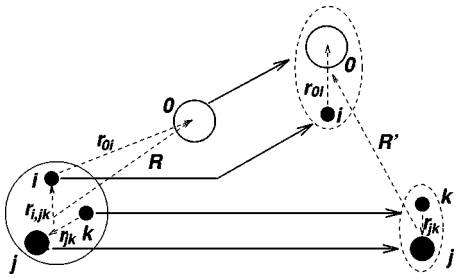

FIG. 1. Sketch of the reaction and coordinates used. The target is labeled by 0 and $\{i,j,k\}$ label the particles within the three-body projectile. Compare with Eq. (1).

II. MODEL AND METHOD

The spatially extended three-body halo collides with a relatively small target at high energy. Then the probability that more than one of the constituents interacts strongly with the target is small. The differential cross section $d\sigma$ is then to a good approximation a sum of three terms $d\sigma^{(i)}$ each describing the independent contribution to the process from the interaction between the target and the halo particle i. This is the assumption used in the classical formulation for a weakly bound projectile [32]. We neglect the binding energy of the initial three-body bound state compared to the high energy of the beam. The reaction is then described as three particles independently interacting with the target as if each particle were free.

The process is described as removal of one particle i (participant) while the other two particles j and k (spectators) both survive the reaction undisturbed (see Fig. 1). The participant is either absorbed (stripped) or elastically scattered (diffracted) by the target. The final state then consists of two independent subsystems, i.e., the target plus participant and the two spectators. The interaction in the final state between the two spectators j and k must be the same as in the initial three-body bound state. This consistency is previously only reported in Refs. [21,22].

We shall first show how to compute fragmentation cross sections of two-neutron halo nuclei on light targets where the Coulomb interaction is negligibly small. We then briefly describe how the wave functions in the initial and final states are constructed. Finally we give the various interactions used in the calculations.

A. Cross sections

The masses and the coordinates and their conjugate momenta are denoted m, $\boldsymbol{r}$, and $\boldsymbol{p}$, respectively. The three halo particles and the target are labeled by $\{i,j,k\}=\{1,2,3\}$ and 0, respectively. The relative coordinates $\boldsymbol{r}_{jk}$, $\boldsymbol{r}_{0i}$, $\boldsymbol{r}_{i,jk}$, $\boldsymbol{R}$ and $\boldsymbol{R}'$, see Fig. 1, are defined by

$$\boldsymbol{r}_{jk}=\boldsymbol{r}_j-\boldsymbol{r}_k, \quad \boldsymbol{r}_{0i}=\boldsymbol{r}_0-\boldsymbol{r}_i,$$

$$\boldsymbol{r}_{i,jk}=\boldsymbol{r}_i-\frac{m_j\boldsymbol{r}_j+m_k\boldsymbol{r}_k}{m_j+m_k},$$

$$\boldsymbol{R}\equiv\boldsymbol{r}_{0,ijk}=\boldsymbol{r}_0-\frac{m_i\boldsymbol{r}_i+m_j\boldsymbol{r}_j+m_k\boldsymbol{r}_k}{m_i+m_j+m_k},$$

$$\boldsymbol{R}' \equiv \boldsymbol{r}_{0i,jk} = \frac{m_0\boldsymbol{r}_0 + m_i\boldsymbol{r}_i}{m_0+m_i} - \frac{m_j\boldsymbol{r}_j + m_k\boldsymbol{r}_k}{m_j+m_k}. \tag{1}$$

The corresponding conjugate momenta are analogously denoted by $\boldsymbol{p}_{jk}$, $\boldsymbol{p}_{0i}$, $\boldsymbol{p}_{i,jk}$, $\boldsymbol{p}_{0,ijk}$ and $\boldsymbol{p}_{0i,jk}$, i.e.,

$$\boldsymbol{p}_{jk} = \frac{m_k\boldsymbol{p}_j - m_j\boldsymbol{p}_k}{m_k+m_j}, \quad \boldsymbol{p}_{0i} = \frac{m_i\boldsymbol{p}_0 - m_0\boldsymbol{p}_i}{m_0+m_i},$$

$$\boldsymbol{p}_{i,jk} = \frac{(m_j+m_k)\boldsymbol{p}_i - m_i(\boldsymbol{p}_j+\boldsymbol{p}_k)}{m_i+m_j+m_k},$$

$$\boldsymbol{P} \equiv \boldsymbol{p}_{0,ijk} = \frac{(m_i+m_j+m_k)\boldsymbol{p}_0 - m_0(\boldsymbol{p}_i+\boldsymbol{p}_j+\boldsymbol{p}_k)}{m_0+m_i+m_j+m_k},$$

$$\boldsymbol{p}_{0i,jk} = \frac{(m_j+m_k)(\boldsymbol{p}_0+\boldsymbol{p}_i) - (m_0+m_i)(\boldsymbol{p}_j+\boldsymbol{p}_k)}{m_0+m_i+m_j+m_k}. \tag{2}$$

These momenta are related in the same way for the final states. We use primes to indicate the final state and may therefore add primes on all momenta in Eq. (2). In particular $\boldsymbol{p}'_{jk}$ and $\boldsymbol{p}'_{0i}$ are the relative two-body momenta and $\boldsymbol{P}' \equiv \boldsymbol{p}'_{0i,jk}$ is the conjugate of $\boldsymbol{R}'$ in the final state.

We can now easily express the individual momenta in terms of three relative momenta and one absolute momentum, for example $\boldsymbol{p}_{jk}$, $\boldsymbol{p}_{0i}$, $\boldsymbol{p}_{0,ijk}$ and $\boldsymbol{p}_i+\boldsymbol{p}_j+\boldsymbol{p}_k$. This would be natural for the initial state whereas it is more convenient to use the beam momentum and $\boldsymbol{p}'_{jk}$, $\boldsymbol{p}'_{0i}$, $\boldsymbol{P}'$ in the final state. We shall work in the center of mass system of the projectile where the beam momentum is $-\boldsymbol{p}_0$ and $\boldsymbol{p}_i+\boldsymbol{p}_j+\boldsymbol{p}_k=0$. Using total momentum conservation, $\boldsymbol{p}'_0 = \boldsymbol{p}_0 - \boldsymbol{p}'_i - \boldsymbol{p}'_j - \boldsymbol{p}'_k$, we obtain the individual momenta in the final state as

$$\boldsymbol{p}'_j = \boldsymbol{p}'_{jk} - \frac{m_j\boldsymbol{P}'}{m_j+m_k} + \frac{m_j\boldsymbol{p}_0}{m_0+m_i+m_j+m_k},$$

$$\boldsymbol{p}'_k = -\boldsymbol{p}'_{jk} - \frac{m_k\boldsymbol{P}'}{m_j+m_k} + \frac{m_k\boldsymbol{p}_0}{m_0+m_i+m_j+m_k},$$

$$\boldsymbol{p}'_i = -\boldsymbol{p}'_{0i} + \frac{m_i\boldsymbol{P}'}{m_0+m_i} + \frac{m_i\boldsymbol{p}_0}{m_0+m_i+m_j+m_k},$$

$$\boldsymbol{p}'_0 = \boldsymbol{p}'_{0i} + \frac{m_0\boldsymbol{P}'}{m_0+m_i} + \frac{m_0\boldsymbol{p}_0}{m_0+m_i+m_j+m_k}. \tag{3}$$

The process is described as a participant-target reaction and two undisturbed spectators, i.e., momentum conservation dictates that

$$\boldsymbol{p}'_j + \boldsymbol{p}'_k = \boldsymbol{p}_j + \boldsymbol{p}_k, \quad \boldsymbol{p}'_0 + \boldsymbol{p}'_i = \boldsymbol{p}_0 + \boldsymbol{p}_i. \tag{4}$$

In the rest frame of the projectile $\boldsymbol{p}_j+\boldsymbol{p}_k=-\boldsymbol{p}_i$ and $\boldsymbol{p}_i = \boldsymbol{p}_{i,jk}$. Then Eq. (4) can be rewritten as

$$\boldsymbol{p}_{i,jk} = \boldsymbol{P}' - \frac{m_j+m_k}{m_i+m_j+m_k+m_0}\boldsymbol{p}_0,$$

$$\boldsymbol{p}_{0i} = \frac{m_i+m_j+m_k}{m_i+m_j+m_k+m_0}\boldsymbol{p}_0 - \frac{m_0}{m_i+m_0}\boldsymbol{P}'. \tag{5}$$

Let us now first consider elastic scattering of the participant i by the light target. We denote the initial three-body projectile wave function by $\Psi^{(JM)}(\boldsymbol{r}_{jk},\boldsymbol{r}_{i,jk})$, where J and M are the total angular momentum and its projection on the z axis. The final state outgoing distorted wave functions of the independent participant-target and spectator two-body subsystems are respectively $\phi^{(0i+)}_{\boldsymbol{p}'_{0i}\Sigma'_i}$ and $\phi^{(jk+)}_{\boldsymbol{p}'_{jk}s_{jk}\Sigma_{jk}}$, where $\boldsymbol{s}_{jk} = \boldsymbol{s}_j+\boldsymbol{s}_k, \Sigma_{jk} = \Sigma_j+\Sigma_k$ and s_i and Σ_i are spin and projection quantum numbers of particle i. The corresponding spin functions are $\chi_{s_i\Sigma'_i}, \chi_{s_{jk}\Sigma_{jk}}$, where we for convenience assume a zero spin target. The participant-target interaction is V_{0i}, where we only consider a light target. A possible Coulomb interaction can then be neglected.

The transition amplitude $T^{(i)}$ of the process, where particle i is elastically scattered by the target while particles j and k are undisturbed, is most conveniently computed in the center of mass system of the three-body projectile. Using momentum conservation we obtain

$$T^{(i)} = \langle \phi^{(0i+)}_{\boldsymbol{p}'_{0i}\Sigma'_i} \phi^{(jk+)}_{\boldsymbol{p}'_{jk}s_{jk}\Sigma_{jk}} e^{i\boldsymbol{P}'\boldsymbol{R}'} | V_{0i} | \Psi^{(JM)} e^{i\boldsymbol{P}\boldsymbol{R}} \rangle. \tag{6}$$

This amplitude basically factorizes into participant-target elastic scattering transition amplitude $T^{(0i)}_{\Sigma_i\Sigma'_i}$ and the overlap between initial and final states of the spectators $M^{(JM)}_{s_{jk}\Sigma_{jk}\Sigma_i}$, i.e.,

$$T^{(i)} = \sum_{\Sigma_i} T^{(0i)}_{\Sigma_i\Sigma'_i} M^{(JM)}_{s_{jk}\Sigma_{jk}\Sigma_i}, \tag{7}$$

$$T^{(0i)}_{\Sigma_i\Sigma'_i} = \langle \phi^{(0i+)}_{\boldsymbol{p}'_{0i}\Sigma'_i} | V_{0i} | e^{i\boldsymbol{p}_{0i}\boldsymbol{r}_{0i}} \chi_{s_i\Sigma_i} \rangle, \tag{8}$$

$$M^{(JM)}_{s_{jk}\Sigma_{jk}\Sigma_i} = \langle \phi^{(jk+)}_{\boldsymbol{p}'_{jk}s_{jk}\Sigma_{jk}} e^{i\boldsymbol{p}_{i,jk}\boldsymbol{r}_{i,jk}} \chi_{s_i\Sigma_i} | \Psi^{(JM)} \rangle. \tag{9}$$

In breakup computations, where only absorption is included in the sudden approximation, the transition amplitude is proportional to the overlap $M^{(JM)}_{s_{jk}\Sigma_{jk}\Sigma_i}$, see [21,22]. This previous approximation is therefore still valid provided the elastic scattering process can be neglected. If furthermore the final state interaction between the two spectators is neglected the overlap in Eq. (9) reduces to the Fourier transform of the projectile wave function $\Psi^{(JM)}$. This is the approximation used in the first attempt to understand these fragmentation reactions [3,18–20].

The differential diffraction (elastic scattering) cross section is then given by

$$d^9\sigma^{(i)}_{\rm el} = \frac{2\pi}{\hbar}\frac{1}{v}\frac{\delta(E'_{0i}-E_{0i})}{2J+1} \times \sum_{Ms_{jk}\Sigma_{jk}\Sigma'_i} \left| \sum_{\Sigma_i} T^{(0i)}_{\Sigma_i\Sigma'_i} M^{(JM)}_{s_{jk}\Sigma_{jk}\Sigma_i} \right|^2 d\nu^{(i)}_f, \tag{10}$$

where $v = p_0/m_0$ is the velocity of the target seen from the projectile rest frame and $E_{0i} = p^2_{0i}/2\mu_{0i}$ and $E'_{0i} = p'^2_{0i}/2\mu_{0i}$ are the relative energies of particle i and the target in the initial and final states. We use here the nonrelativistic expressions, since the optical model is nonrelativistic although obtained through a relativistic procedure; see the discussion

later in the paper. The reduced mass of particle i and the target is here denoted μ_{0i}. Then energy conservation demands that $|\boldsymbol{p}_{0i}|=|\boldsymbol{p}'_{0i}|$. The density of final states $d\nu_f^{(i)}$ is given by

$$d\nu_f^{(i)}=\frac{d^3\boldsymbol{p}'_{0i}}{(2\pi\hbar)^3}\frac{d^3\boldsymbol{p}'_{jk}}{(2\pi\hbar)^3}\frac{d^3\boldsymbol{P}'}{(2\pi\hbar)^3}. \tag{11}$$

The differential diffraction cross section in Eq. (10) can now also be rewritten in factorized form. When the participant i has spin 0 or 1/2 and the target has spin 0, we get, as shown in Appendix A, the expression

$$\frac{d^9\sigma_{\rm el}^{(i)}(\boldsymbol{P}',\boldsymbol{p}'_{jk},\boldsymbol{p}'_{0i})}{d\boldsymbol{P}'\,d\boldsymbol{p}'_{jk}d\boldsymbol{p}'_{0i}}=\frac{d^3\sigma_{el}^{(0i)}(\boldsymbol{p}_{0i}\rightarrow\boldsymbol{p}'_{0i})}{d\boldsymbol{p}'_{0i}}|M_s(\boldsymbol{p}_{i,jk},\boldsymbol{p}'_{jk})|^2, \tag{12}$$

where the first factor is the differential cross section for the participant-target elastic scattering process,

$$\frac{d^3\sigma_{\rm el}^{(0i)}(\boldsymbol{p}_{0i}\rightarrow\boldsymbol{p}'_{0i})}{d\boldsymbol{p}'_{0i}}=\frac{1}{v}\frac{2\pi}{\hbar}\frac{\delta(E'_{0i}-E_{0i})}{(2\pi\hbar)^3}\frac{1}{2s_i+1}\sum_{\Sigma_i\Sigma'_i}|T^{(0i)}_{\Sigma_i\Sigma'_i}|^2, \tag{13}$$

and the second factor is the overlap matrix element used in the original formulation of the sudden approximation for absorption [21,22]

$$|M_s(\boldsymbol{p}_{i,jk},\boldsymbol{p}'_{jk})|^2\equiv\frac{1}{2J+1}\sum_{Ms_{jk}\Sigma_{jk}\Sigma_i}|M^{(JM)}_{s_{jk}\Sigma_{jk}\Sigma_i}|^2, \tag{14}$$

which is normalized to one, i.e., gives unity after integration over $\boldsymbol{p}_{i,jk}$ and $\boldsymbol{p}'_{jk}$ or equivalently, by use of Eq. (5), over $\boldsymbol{P}'$ and $\boldsymbol{p}'_{jk}$.

We also consider the other process, where the participant in the sense of the optical model is absorbed by the target. We obtain analogously the corresponding differential absorption (stripping) cross section in the same factorized form

$$\frac{d^6\sigma_{\rm abs}^{(i)}(\boldsymbol{P}',\boldsymbol{p}'_{jk})}{d\boldsymbol{P}'\,d\boldsymbol{p}'_{jk}}=\sigma_{\rm abs}^{(0i)}(p_{0i})|M_s(\boldsymbol{p}_{i,jk},\boldsymbol{p}'_{jk})|^2, \tag{15}$$

where $\sigma_{\rm abs}^{(0i)}$ is the participant-target absorption cross section. The nine-dimensional differential cross section is now reduced to six, since the absorbed or stripped particle inherently is of no interest in the optical model description.

It is conceptually important to realize that the factorizations in Eqs. (12) and (15) are incomplete, since $\boldsymbol{p}_{0i}$ in the participant-target cross sections is related to $\boldsymbol{P}'$ or $(\boldsymbol{p}_{i,jk})$ in Eq. (14) via the momentum conservation in Eq. (5). For high energy reactions the factorization is in practice fairly accurate for two reasons. First the range of p_{0i} values is limited to an interval around $[m_i/(m_0+m_i)]p_0$ determined by the size of the relatively small momenta in the motion of the particles within the projectile; see Eq. (2). Second the factor arising from the participant-target cross section depends only weakly on energy for the large beam energies corresponding to this rather small range of p_{0i} values.

Computations of the fragmentation cross sections are now essentially reduced to computations of the overlap matrix element $M^{(JM)}_{s_{jk}\Sigma_{jk}\Sigma_i}$ from [22] (modified to account for shadowing by omission of the unwanted configurations) and the two-body elastic and absorption cross sections determined by the optical model phase shifts. A target with zero spin, e.g., an even-even nucleus like ^{12}C, and a neutron with spin 1/2 as the participant particle is of particular interest for halo nuclei. We then have [33]

$$\frac{d^3\sigma_{\rm el}^{(0i)}(\boldsymbol{p}_{0i}\rightarrow\boldsymbol{p}'_{0i})}{d\boldsymbol{p}'_{0i}}=\frac{\delta(E'_{0i}-E_{0i})}{\mu_{0i}^2v}(|g(p_{0i},\theta)|^2+|h(p_{0i},\theta)|^2), \tag{16}$$

$$\sigma_{\rm abs}^{(0i)}(p_{0i})=\frac{\pi}{p_{0i}^2}\sum_{l=0}^{\infty}[(2l+1)-(l+1)|e^{2i\delta_l^{(l+1/2)}}|^2-l|e^{2i\delta_l^{(l-1/2)}}|^2], \tag{17}$$

where θ is the angle between $\boldsymbol{p}_{0i}$ and $\boldsymbol{p}'_{0i}$ and $\delta_l^{(j)}$ is the phase shift of the partial wave l when the total angular momentum is j. The functions g and h are given by

$$g(p_{0i},\theta)=\frac{1}{2ip_{0i}}\sum_{l=0}^{\infty}[(l+1)(e^{2i\delta_l^{(l+1/2)}}-1)+l(e^{2i\delta_l^{(l-1/2)}}-1)]P_l(\cos\theta), \tag{18}$$

$$h(p_{0i},\theta)=\frac{1}{2p_{0i}}\sum_{l=1}^{\infty}(e^{2i\delta_l^{(l+1/2)}}-e^{2i\delta_l^{(l-1/2)}})\times\sin\theta\frac{d}{d(\cos\theta)}P_l(\cos\theta), \tag{19}$$

where P_l is the lth Legendre polynomial.

The two contributions (stripping and diffraction or absorption and scattering) arising from the interaction V_{0i} to any measurable cross section is now obtained by integration over the unobserved momenta in Eqs. (12) and (15). The total cross section is given by the sum of both contributions and the weight of each of them is directly dictated by the optical potential. We shall compute individual as well as relative momentum distributions in the final state both along $\boldsymbol{p}_0$ (longitudinal) and perpendicular to $\boldsymbol{p}_0$ (transverse).

In addition to momentum distributions we shall also compute other observables like the invariant mass spectrum of the two particles in the final state. This mass is invariant under Lorentz transformations and therefore independent of coordinate system. In particular, in the rest system for the particles j and k the invariant mass reduces for the relevant small energies to the nonrelativistic kinetic energy $E_{jk}=E'_{jk}=p'^2_{jk}/2\mu_{jk}$ of this two-body system. Then the momentum variable p'_{jk} can be substituted by E_{jk} by use of $dE_{jk}=p'_{jk}dp'_{jk}/\mu_{jk}$.

Another recently investigated observable is the angular distribution of the relative momentum between the spectators j and k in a coordinate system with the z axis along the center of mass of their total momentum in the final state. The decisive variable is then the angle between $\boldsymbol{p}'_{jk}$ and $\boldsymbol{p}'_j+\boldsymbol{p}'_k=-\boldsymbol{p}_i=-\boldsymbol{p}_{i,jk}$, where the latter vector is given in Eq. (5). To

compute this angular distribution we express the differential cross sections as functions of $-\boldsymbol{p}_{i,jk}$ and $\boldsymbol{p}'_{jk}$ and integrate over all the variables except the angle between these two vectors.

The necessary integrations require variable changes in the description of the final state. The expressions in Eq. (3) provide useful identities for this purpose, i.e.,

$$\frac{d^9\sigma^{(i)}_{\rm el}(\boldsymbol{P}',\boldsymbol{p}'_{jk},\boldsymbol{p}'_{0i})}{d\boldsymbol{P}'\,d\boldsymbol{p}'_{jk}d\boldsymbol{p}'_{0i}}=\frac{d^9\sigma^{(i)}_{\rm el}(\boldsymbol{P}',\boldsymbol{p}'_{j},\boldsymbol{p}'_{0i})}{d\boldsymbol{P}'\,d\boldsymbol{p}'_{j}d\boldsymbol{p}'_{0i}}=\frac{d^9\sigma^{(i)}_{\rm el}(\boldsymbol{P}',\boldsymbol{p}'_{k},\boldsymbol{p}'_{0i})}{d\boldsymbol{P}'\,d\boldsymbol{p}'_{k}d\boldsymbol{p}'_{0i}}$$
$$=\frac{d^9\sigma^{(i)}_{\rm el}(\boldsymbol{P}',\boldsymbol{p}'_{jk},\boldsymbol{p}'_{i})}{d\boldsymbol{P}'\,d\boldsymbol{p}'_{jk}d\boldsymbol{p}'_{i}}, \tag{20}$$

$$\frac{d^6\sigma^{(i)}_{\rm abs}(\boldsymbol{P}',\boldsymbol{p}'_{jk})}{d\boldsymbol{P}'\,d\boldsymbol{p}'_{jk}}=\frac{d^6\sigma^{(i)}_{\rm abs}(\boldsymbol{P}',\boldsymbol{p}'_{j})}{d\boldsymbol{P}'\,d\boldsymbol{p}'_{j}}=\frac{d^6\sigma^{(i)}_{\rm abs}(\boldsymbol{P}',\boldsymbol{p}'_{k})}{d\boldsymbol{P}'\,d\boldsymbol{p}'_{k}}. \tag{21}$$

We have so far only considered the two contributions coming from the stripping and the diffraction of particle i via the interaction V_{0i}. However, the reaction in question may also be a result of the other interactions V_{0j} or V_{0k}. These cross sections are then simply added. Possible interference terms are neglected, since they in any case are small for spatially extended projectiles. From Eqs. (12) and (15) we expect that the absolute values all are of the same order of magnitude as the corresponding participant-target cross sections.

B. Wave functions and shadowing

The initial three-body wave function $\Psi^{(JM)}$ of the projectile is obtained by solving the Faddeev equations in coordinate space [4]. We use the three sets of hyperspherical coordinates $(\rho,\Omega_i),\Omega_i=\{\alpha_i,\Omega_{xi},\Omega_{yi}\}$, where each i is related to a given Jacobi system; see [3,4]. Then $\Psi^{(JM)}$ is a sum of the three Faddeev components, which in turn for each hyperradius ρ are expanded in a complete set of generalized angular functions $\Phi^{(i)}_n(\rho,\Omega_i)$

$$\Psi^{JM}=\frac{1}{\rho^{5/2}}\sum_n f_n(\rho)\sum_{i=1}^{3}\Phi^{(i)}_n(\rho,\Omega_i), \tag{22}$$

where $\rho^{-5/2}$ is related to the volume element $\rho^5 d\rho\, d\Omega_i$ with the angular part $d\Omega_i=\sin^2\alpha_i\cos^2\alpha_i d\alpha_i d\Omega_{xi}d\Omega_{yi}$.

These angular wave functions satisfy the angular part of the three Faddeev equations, i.e.,

$$\frac{\hbar^2}{2m}\frac{1}{\rho^2}\hat{\Lambda}^2\Phi^{(i)}_n+V_{jk}(\Phi^{(i)}_n+\Phi^{(j)}_n+\Phi^{(k)}_n)\equiv\frac{\hbar^2}{2m}\frac{1}{\rho^2}\lambda_n(\rho)\Phi^{(i)}_n, \tag{23}$$

where $\{i,j,k\}$ is a cyclic permutation of $\{1,2,3\}$, m is a normalization mass, V_{jk} is the two-body interaction between particles j and k, and $\hat{\Lambda}^2$ is the ρ-independent part of the kinetic energy operator. The analytic expressions for $\hat{\Lambda}^2$ and the kinetic energy operator can, for instance, be found in [4].

The radial expansion coefficients $f_n(\rho)$ are obtained from the coupled set of ''radial'' differential equations [4]

$$\left(-\frac{d^2}{d\rho^2}-\frac{2m(E-V_3(\rho))}{\hbar^2}+\frac{\lambda_n(\rho)}{\rho^2}+\frac{15}{4\rho^2}-Q_{nn}\right)f_n(\rho)$$
$$=\sum_{n'\neq n}\left(2P_{nn'}\frac{d}{d\rho}+Q_{nn'}\right)f_{n'}(\rho), \tag{24}$$

where V_3 is an anticipated three-body potential and the functions P and Q are defined as the angular integrals

$$P_{nn'}(\rho)\equiv\sum_{i,j=1}^{3}\int d\Omega\,\Phi^{(i)}_n{}^*(\rho,\Omega)\frac{\partial}{\partial\rho}\Phi^{(j)}_{n'}(\rho,\Omega), \tag{25}$$

$$Q_{nn'}(\rho)\equiv\sum_{i,j=1}^{3}\int d\Omega\,\Phi^{(i)}_n{}^*(\rho,\Omega)\frac{\partial^2}{\partial\rho^2}\Phi^{(j)}_{n'}(\rho,\Omega). \tag{26}$$

The continuum wave function $\phi^{(jk+)}_{\boldsymbol{p}'_{jk}s_{jk}\Sigma_{jk}}$ describing the two-body spectator system in the final state is expanded in partial waves [22]

$$\phi^{(jk+)}_{\boldsymbol{p}'_{jk}s_{jk}\Sigma_{jk}}=\sqrt{\frac{2}{\pi}}\frac{1}{p'_{jk}r_{jk}}\sum_{j_{jk}l_{jk}m_{jk}}u^{j_{jk}}_{l_{jk}s_{jk}}(p'_{jk},r_{jk})$$
$$\times\mathcal{Y}^{m_{jk}*}_{j_{jk}l_{jk}s_{jk}}(\Omega_{r_{jk}})\sum_{m_{l_{jk}}=-l_{jk}}^{l_{jk}}i^{l_{jk}}Y_{l_{jk}m_{l_{jk}}}(\Omega_{p'_{jk}})$$
$$\times\langle l_{jk}m_{l_{jk}}s_{jk}\Sigma_{jk}|j_{jk}m_{jk}\rangle, \tag{27}$$

where $\langle|\rangle$ is a Clebsch-Gordon coefficient, Y_{lm_l} is the spherical harmonic and $\mathcal{Y}^{m*}_{jls}(\Omega_r)$ is the angular wave function obtained by coupling orbital l and spin s to the total angular momentum and projection j and m. The distorted radial wave functions $u^{j_{jk}}_{l_{jk}s_{jk}}(p'_{jk},r_{jk})$ are obtained by solving the Schrödinger equation with the appropriate two-body potential. When this interaction between the two spectators in the final state is neglected the expansion in Eq. (27) reduces to the usual expansion of plane waves in terms of spherical Bessel functions.

The participant-target interaction is described by the optical potential while the spectators remain unaffected. The finite extension of the projectile and the target therefore in addition requires exclusion of configurations where the spectators pass the target too close to the participant. This corresponds to black sphere models describing the spectator-target interactions. This so-called shadowing strictly requires exclusion of the initial projectile wave function in an infinitely long cylinder with the axis along the motion of the participant. However, such a cylinder depends on the dynamics of the reaction and omission of these events would be technically difficult in large scale systematic computations. Instead we approximate the shadowing by excluding spheres of the wave function where the participant is close to the spectators. This is much simpler and has also the appealing feature that major parts of the three-body wave function describing configurations, where the spatially extended particles are inside the radii of each other, simultaneously are excluded. Then the contribution from densities, where halo and core nucleons overlap, decreases and consequently the possible uncer-

tainty due to the treatment of the Pauli principle must be diminished or perhaps completely eliminated [34].

Thus we account for the shadowing effect by substituting zero for the initial three-body wave function $\Psi^{(JM)}$ when the distances between participant i and the two spectators j and k are smaller than the shadowing parameters $r_{nc}^{(ij)}$ and $r_{nn}^{(ik)}$, respectively. Here we indicated that one neutron reacts with the target while the core and the other neutron are spectators. Instead of this sharp cutoff a smooth function, varying from zero at small distances to one at large distances, could easily be used to eliminate the unwanted geometric configurations. The cutoff radii are in any case related to the sizes of target and spectators. With the core or nucleon as spectators a reasonable parametrization could then be

$$r_{nc}=r_0\sqrt{A_t^{2/3}+A_c^{2/3}}, \quad r_{nn}=\sqrt{r_0^2A_t^{2/3}+R_N^2}, \tag{28}$$

where for simplicity we omitted the superscripts ij and ik. The mass numbers of target and core are A_t and $A_c(A_c=9$ for ^{11}Li) and $R_N\approx 1$ fm is the sharp cutoff radius of the nucleon. We choose the parameter $r_0\approx 1.26$ fm, which is adjusted to reproduce the few reported absolute values of two-neutron removal cross sections. This somewhat large value of r_0 may reflect a parametrization where the range of the nuclear interaction is included. The shadowing effect substantially reduces the absolute values of the cross sections [24,26]. This sensitivity in addition to the approximate nature of the treatment of shadowing indicates that the predicted absolute values are less accurate than desired. On the other hand, the shapes of the distributions are fairly insensitive to the shadowing parameters although the effects are significant at the present level of accuracy.

C. Interaction parameters

The model described in the previous subsections needs specifications of the interactions appropriate for the process under investigation. We shall here focus on the fragmentation of a ^{11}Li(^{9}Li$+n+n$) projectile on a carbon target and divide the parameters into five sets, i.e., (i) the four two-body interactions between neutron-neutron, (ii) neutron-^{9}Li, (iii) neutron-carbon, (iv) ^{9}Li-carbon two-body systems, and (v) the three-body interaction for the ^{11}Li three-body system.

The neutron-neutron interaction V_{nn} contains central, spin-orbit, tensor and spin-spin interactions, i.e.,

$$V_{nn}(r)=V_c(r)+V_{ss}(r)\boldsymbol{s}_1\cdot\boldsymbol{s}_2+V_T(r)S_{12}+V_{so}(r)\boldsymbol{l}_{nn}\cdot\boldsymbol{s}_{nn}, \tag{29}$$

where $\boldsymbol{l}_{nn}$ is the relative orbital angular momentum, S_{12} is the tensor operator, $\boldsymbol{s}_1$ and $\boldsymbol{s}_2$ are the spins of the two neutrons and $\boldsymbol{s}_{nn}=\boldsymbol{s}_1+\boldsymbol{s}_2$. We assume Gaussian shapes for each of the radial potentials $V(r)$. The parameters are adjusted to reproduce the experimental low-energy neutron-neutron scattering data for s and p waves. Different radial shapes and in general more elaborate potentials have previously been used in the present context. The results are essentially indistinguishable from each other provided the scattering lengths and effective ranges remain unchanged. We shall therefore use the interactions specified in [34], where the corresponding s and p-wave scattering lengths and effective ranges also are given.

The *neutron-^{9}Li interaction* is not very well known, although several pieces of information are available. The low-energy properties are almost exclusively determined by s and p waves and we shall therefore only include these lowest partial waves. The neutron $p_{3/2}$ state is bound by about 4 MeV in ^{9}Li and due to Pauli blocking this state is unavailable for the valence neutron. We are then left with the $s_{1/2}$ and $p_{1/2}$ states. The total neutron angular momentum of 1/2 for each of these states then couple to the ^{9}Li spin of 3/2 resulting in two pairs of spin-split states with angular momenta 1 and 2 and parities corresponding to s and p states, respectively.

The interaction in the present three-body calculations are determined by the low-energy scattering properties, which in turn determine positions and widths of resonances and virtual states. These positions are in fact the decisive properties of the interaction and the parametrization of the force is in itself rather unimportant. We have therefore basically only four parameters of physical importance, i.e., the four positions of the s and p states. Furthermore, the fragmentation results are only sensitive to the statistically averaged positions of the s and p states, i.e., the spin-splitting, almost unavoidable for the strong interaction, does not significantly influence the computed differential cross sections, see the next section. The relative position of the s and p states determines the p^2 content in the three-body wave function of ^{11}Li. The s and p wave content are roughly believed to be of the same order as shown in both calculations and interpretations of experimental fragmentation data [10,14,18,21,22,24,35]. This amount of p-wave admixture strongly influences the fragmentation cross sections, which in addition also are very sensitive to the binding energy or equivalently to the radius of ^{11}Li.

Thus we have two crucial parameters (s and p-state positions) and two sensitive observables (three-body binding and p-wave content). However, this perfect match is upset by additional experimental information, especially knowledge about a p resonance in the neutron-^{9}Li system [14,36–39]. As we shall see all three experimental constraints can only be reproduced simultaneously by use of a three-body interaction, which then is constructed to add the missing binding energy in the three-body system.

We shall therefore first concentrate on the neutron-^{9}Li two-body system. We assume central, spin-spin and spin-orbit terms in the neutron-core interaction, i.e.,

$$V_{nc}^{(l)}(r)=V_c^{(l)}(r)+V_{ss}^{(l)}(r)\boldsymbol{s_n}\cdot\boldsymbol{s}_c+V_{so}^{(l)}(r)\boldsymbol{l}_{nc}\cdot\boldsymbol{s}_n, \tag{30}$$

where $\boldsymbol{l}_{nc}$ is the relative orbital angular momentum, $\boldsymbol{s}_n$ and $\boldsymbol{s}_c$ are the intrinsic spins of the neutron and the core. As for the neutron-neutron interaction the radial potentials $V(r)\propto\exp(-r^2/b^2)$ are Gaussians, adjusted independently for each partial wave.

We choose a large inverse spin-orbit strength to make the $p_{3/2}$ interaction sufficiently repulsive to avoid any contribution of this partial wave in the three-body wave function. Furthermore we shall use a shallow s-wave potential without bound states. This automatically excludes the lowest Pauli forbidden neutron-core s-state from the three-body wave function [3,34].

As an important constraint we shall use the ''strong evidence'' for a p resonance at 538 ± 62 keV with a width of 358 ± 23 keV [38]. We then place the lowest $p_{1/2}$ resonance at 0.5 MeV with a width of 0.4 MeV consistent with the experimental values. We choose rather arbitrarily the total spin of this state to be 1. The range of the Gaussian interaction is in this way determined to be $b=2.55$ fm. A different range produces different widths of the resonances. We then continue again somewhat arbitrarily by placing the other $p_{1/2}$ resonance at 0.92 MeV. To get a potential at the limit without a three-body potential we determine the statistically averaged position of the two $s_{1/2}$ states to be at 350 keV such that the experimental ^{11}Li binding energy is reproduced. This fixes the strength of the s interaction when we use the same range as for the p interaction. Finally we use the spin-spin interaction to place the lowest $s_{1/2}$ state of total spin 2 at an energy of 230 keV. This potential, labeled II, leads to a 30% p-wave content in the ^{11}Li wave function. We could as well have chosen the lowest $s_{1/2}$ state with total spin 1 at the same energy of 230 keV. The results for such a potential would be indistiguishable provided that the average energy of the $s_{1/2}$ states is the same [22].

We could also have chosen a different position for the highest $p_{1/2}$ state. However, a lower value than 0.92 MeV would place the two $p_{1/2}$ states rather close. A higher value would require a lower statistically averaged position of the $s_{1/2}$ states, provided the ^{11}Li binding energy remains unchanged, and the resulting p-wave content then becomes unreasonably small (below 30%) in disagreement with the fragmentation data [10,14,24].

We can now increase the p-wave content by increasing the statistically averaged position of the $s_{1/2}$ states while the parameters for the p waves remain unchanged. The resulting underbinding of ^{11}Li must then be compensated by an attractive three-body force. In this way we construct potential I with 40% p-wave content. Again we could have chosen a different position for the highest $p_{1/2}$ state while maintaining a reasonable p-wave content between 35% and 40%. However, a lower value would then require a lower statistically averaged position of the $s_{1/2}$ states and a repulsive three-body force in order to get the correct ^{11}Li binding energy. A higher value would require a rather high statistically averaged position of the $s_{1/2}$ states, i.e., close or even above the statistical average of the $p_{1/2}$ states. The freedom in choosing the positions of the resonances and virtual states is in fact limited.

The parameters of the potentials I and II are given in Table I along with the p-wave content and the energies of the resonances and virtual states. The statistically averaged position of the two virtual s states in ^{10}Li is higher for potential I than for potential II resulting in the correspondingly larger p-wave content.

In Table I we also for comparison give the parameters corresponding to the neutron-^{9}Li interaction (called III) used in [40,41]. The main difference compared to potentials I and II is that the lowest p resonance is placed at 0.75 MeV with a width of 0.87 MeV. Maintaining the p interaction and increasing the p-wave content to about 40% would require a statistically averaged position of the s states above the corresponding average position of the p states. This is the reason for the choice of the slightly lower value of 0.5 MeV for the lowest p state. Potential I is a rather good starting point. To investigate the effects of spin splitting we also constructed the potentials IV and V, where the statistically averaged positions of the s and p waves are maintained. Then the p-wave content and the ^{11}Li binding energy is also unchanged.

TABLE I. Parameters for various neutron-^{9}Li interactions. The form is given in Eq. (30) and the radial shapes are all Gaussians, $\exp(-r^2/b^2)$, with ranges $b=2.55$ fm and strengths denoted by $V_c^{(l)}$, $V_{ss}^{(l)}$, and $V_{so}^{(l)}$ with $l=0,1$ for s and p waves, respectively. The strength parameter for the corresponding three-body interaction, $V_3\exp(-\rho^2/b_3^2)$ with $b_3=2.50$ fm, are also given. The lower part of the table contains p-wave content in % in the ^{11}Li wave function and the four energies of the resonances and virtual states $E_{s_{1/2}}^{(1)}$, $E_{s_{1/2}}^{(2)}$, $E_{p_{1/2}}^{(1)}$, and $E_{p_{1/2}}^{(2)}$. All the energies and strengths are given in MeV, and the ranges in fm. All potentials are defined in the text except III which is from [40].

	I	II	III	IV	V
$V_c^{(0)}$	−5.60	−6.42	−7.28	−5.60	−5.60
$V_{ss}^{(0)}$	−1.75	−0.75	−0.31	0.00	−3.00
$V_c^{(1)}$	−5.00	−5.00	18.25	−5.00	−5.00
$V_{ss}^{(1)}$	1.00	1.00	1.47	0.00	2.00
$V_{so}^{(1)}$	33.60	33.60	55.00	33.60	33.60
V_3	−3.75	0.00	0.00	−3.75	−3.75
p^2(%)	40	30	20	40	40
$E_{s_{1/2}}^{(2)}$	0.24	0.23	0.14	0.58	0.09
$E_{s_{1/2}}^{(1)}$	1.49	0.62	0.25	0.58	2.37
$E_{p_{1/2}}^{(1)}$	0.50	0.50	0.75	0.75	0.27
$E_{p_{1/2}}^{(2)}$	0.92	0.92	1.60	0.75	1.13

In conclusion, the neutron-^{9}Li potential is already rather severely constrained by existing data. The lowest $p_{1/2}$ state is experimentally determined to be around 0.5 MeV. The ground state is an s state. The distance between the statistically averaged positions for the $s_{1/2}$ and $p_{1/2}$ states is determined by the requirement of about 40% p-wave content of the neutron-core relative motion in the total ^{11}Li wave function. For example maintaining the ^{11}Li binding energy at around 300 keV, the p-wave content around 40% and the three-body force in potential I, a $p_{1/2}$ average energy at around 0.65 MeV would require the $s_{1/2}$ average energy at roughly the same value. If the lowest $p_{1/2}$ state is at 0.5 MeV the highest $p_{1/2}$ state has to be above 0.72 MeV, because the $p_{1/2}$ average energy otherwise would fall below the $s_{1/2}$ average energy. In the same way, a low $s_{1/2}$ state close to zero requires the highest $s_{1/2}$ state below 1.7 MeV to avoid the same inversion.

The *three-body interaction* is chosen as $V_3\exp(-\rho^2/b_3^2)$, where $b_3=2.50$ fm and the strength V_3 is adjusted to reproduce the measured two-neutron separation energy for ^{11}Li, i.e., 295 ± 35 keV. This additional force is necessary, since the two-body interactions reproducing all low-energy scattering phase shifts lead to an underbinding of the three-body system. For ^{6}He this deficiency amounts to around 0.5 MeV [41,42]. The idea is that the three-body force should account for the polarization of the particles beyond that described by the two-body interactions. Then all three particles must be

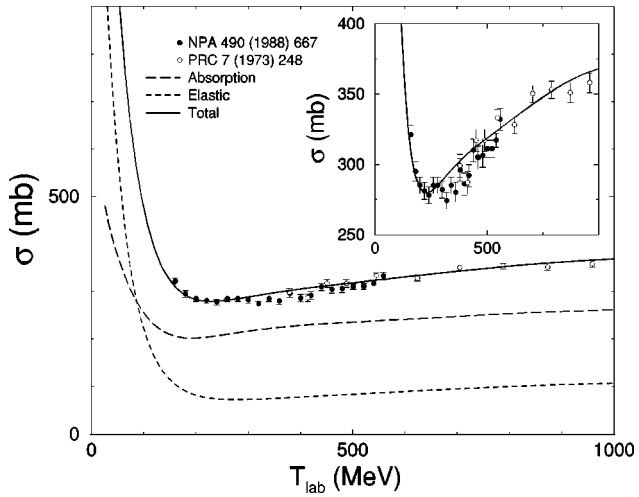

FIG. 2. The total (solid), elastic (dashed), and absorption (short-dashed) cross sections σ for neutron-^{12}C reactions as functions of the neutron laboratory kinetic energy $T_{\rm lab}$. The inset focuses on the region of the minimum. The open and filled circles are experimental points from [46,47], respectively. The curves are obtained in an optical model computation as decribed in [44] using the parameters in [28]. We include 35 partial waves in the calculations.

close to produce this additional polarization or modification of the intrinsic structure of the composite particles. Thus the three-body force must be of short range.

The importance of the three-body interaction is perhaps seen most clearly in three-body continuum calculations where the resonance structure of the two-body subsystems probably is decisive. The three-body force is designed to give the correct three-body binding energy while the two-body interactions remain unchanged still reproducing the two-body structure. With the correct two-body interactions the computed three-body continuum structure is much more reliable [43].

For the *neutron-carbon interaction* we use nonrelativistic optical potentials obtained from relativistic potentials through a reduction of the Dirac equation into a Schrödinger-like equation [44]. These phenomenological potentials in the Schrödinger equation produce the same scattering data as obtained by use of the relativistic potentials in the Dirac equation [45].

In particular for a carbon target the interaction used is the parametrization EDAI-C12 [28] valid for a range of neutron kinetic energies from 29 to 1040 MeV. The resulting neutron-^{12}C cross sections are shown in Fig. 2. For energies above 150 MeV the cross sections are relatively weak functions of energy and absorption is much more likely than diffraction. The factorization of the fragmentation cross sections in Eqs. (12) and (15) is then rather accurate at these high energies.

At energies below 150 MeV the neutron-target cross sections increase dramatically. The factorization is then less accurate, but still a useful approximation. Furthermore, diffraction quickly dominates over absorption. The absolute cross sections for fragmentation of ^{11}Li can then be expected to increase with decreasing beam energy. The shapes of the distributions also should change from narrow (absorption) to broad (elastic scattering) with decreasing energy. At intermediate energies we can expect a mixture exhibiting a narrow distribution with a relatively large broad background. These predictions are simple consequences of the model, where the fragmentation cross sections essentially are proportional to the neutron-carbon cross sections.

The *carbon-^{9}Li interaction* is needed to estimate the cross sections both when the ^{9}Li core is destroyed (absorped) and the two neutrons detected and when the core is scattered (diffracted) on the target. These cross sections are obtained by a two-body computation of the carbon-^{9}Li reactions using the simple almost schematic optical potential defined in [48] and described in [49]. In this model the beam energy dependence is introduced through the proton-proton and neutron-proton cross sections. Experimental data of these nucleon-nucleon cross sections can be found in [50].

In the calculation of the ^{9}Li-^{12}C cross section we assume spin zero for ^{9}Li. We need around 150 partial waves to get convergence. At a beam energy of 280 MeV/nucleon the computed elastic cross section is 419 mb and the computed absorption cross section is 795 mb. This gives a total of 1214 mb consistent with the results in [51]. These values are dramatically reduced by the shadowing effect.

III. COMPARISON WITH EXPERIMENTS

The interaction parameters discussed in the previous section determine the structure of the three-body projectile. The positions of the resonances and the *p*-wave content are the crucial quantities. The reactions are described by the participant-target interactions and the cutoff radii taking the shadowing effect into account. We previously used the cutoff radii $r_{nc}=r_{nn}=3$ fm [27], which is consistent with the fragmentation data for ^{6}He on carbon [26]. For ^{11}Li fragmentation the neutron-neutron shadowing parameter should remain the same, since the physical origin is unchanged. Therefore we use $r_{nn}=3$ fm while we still maintain the neutron-^{9}Li shadowing radius r_{nc} as a parameter for adjustments within rather narrow limits around the value obtained from Eq. (28). The radius of ^{9}Li is 0.9 fm larger than the radius of ^{4}He and the value of r_{nc} is then expected to be about 4 fm for ^{11}Li. In this section we shall compute different types of observables as discussed in the previous section and use the experimental data to select a promising set of interactions and shadowing parameters. We shall only display results for potentials I, II and III and omit the curves for potentials IV and V, which in all cases barely can be distinguished from those of I.

The *two-neutron removal cross section* σ_{-2n} is known experimentally for ^{11}Li fragmentation on a carbon target at 280 MeV/nucleon [14]. All events, where ^{9}Li is detected after the fragmentation, contribute to this cross section. According to [14] three different reaction mechanisms lead to such a halo breakup. First electromagnetic excitation of the halo state into the continuum followed by decay of these excited states. We shall neglect this process, since it is expected to give a rather small contribution (less than 10 mb) for a light target like carbon.

The second mechanism is the stripping of one of the halo neutrons by the target. This process is also called absorption and the corresponding cross section is denoted by σ^S_{-2n}. It is fully described in our model via the imaginary part of the neutron-target optical potential. On the other hand, we neglect processes where both neutrons are absorbed by the tar-

TABLE II. Core diffraction (σ^{CD}_{-2n}), two-neutron removal cross sections (σ_{-2n}) equal to the sum of neutron diffraction (σ^{D}_{-2n}) and neutron stripping (σ^{S}_{-2n}) computed for fragmentation of ^{11}Li at an energy of 280 MeV/nucleon. The lowest part of the table is for an aluminum target whereas everything else refers to a carbon target. The cross sections are in millibarns. The potentials and shadowing parameters are from Table I. The experimental data are from [14] and [12] for carbon and aluminum, respectively. Potentials IV and V produce the same values as potential I.

Int	r_{nc}	r_{nn}	σ^{CD}_{-2n}	σ^{D}_{-2n}	σ^{S}_{-2n}	σ_{-2n}
	C			80 ± 20	200 ± 20	280 ± 30
I	0	0	88	146	437	583
II	0	0	88	146	437	583
III	0	0	89	145	436	581
I	3.5	3	63	68	204	272
II	3.5	3	65	72	215	287
III	3.5	3	65	76	227	303
I	4	3	52	61	184	245
II	4	3	55	65	195	260
III	4	3	55	69	207	276
	Al					470 ± 80
I	0	0	107	358	901	1259
I	4	3	70	150	379	529
I	5	4	52	100	251	351
I	6	5	38	68	172	240

get and no neutrons appear in the final state. This contribution to the cross section is expected to be small, since the large spatial extension of the projectile diminishes these simultaneous reactions.

The third mechanism is the diffraction of one of the halo neutrons. We also refer to this process as elastic scattering and we denote the corresponding cross section by σ^{D}_{-2n}. For weakly bound systems and not too small beam energy the main contribution to σ^{D}_{-2n} comes from processes where the neutron after scattering on the target ceases to interact with the remaining two halo particles. This is precisely our model, where the final state is described as two independent two-body systems and the interaction between them is ignored, see Fig. 1.

In addition to these three mechanisms there must be a contribution (σ^{CD}_{-2n}) where the core is scattered by the target. In Table II we give these computed cross sections for the potentials in Table I and different sets of shadowing parameters. It is remarkable that the cross sections calculated without shadowing are virtually independent of the potentials, and furthermore clearly much larger than observed. The computed values are reduced by roughly a factor of two by using the shadowing parameters $r_{nc}=3.5$ fm and $r_{nn}=3$ fm. Then by neglecting the two-neutron absorption (not computed) and the core diffraction processes the experimental numbers are reproduced within the error bars for the total as well as for the stripping and diffraction cross sections. Therefore we should underestimate the experimental values and use the larger shadowing parameters $r_{nc}=4$ fm and $r_{nn}=3$ consistent with the parametrization in Eq. (28).

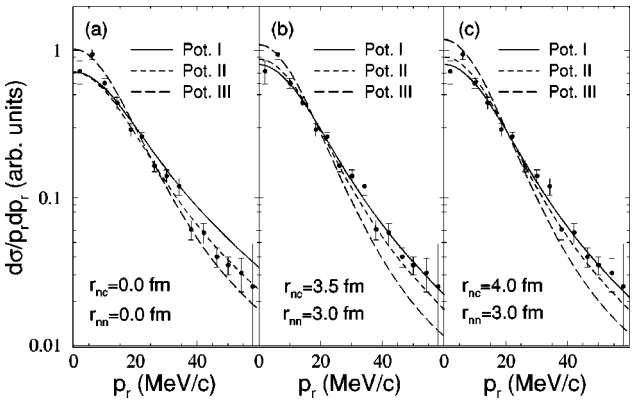

FIG. 3. Radial neutron momentum distribution after fragmentation of ^{11}Li on a carbon target at 280 MeV/nucleon. Core diffraction is not included. The experimental data from [10] is compared with calculations using the potentials I (solid), II (short-dashed), and III (long-dashed) in Table I. The shadowing parameters are given in the figure. The optical model parameters are from [28].

However, the computed core diffraction contributions in Table II are not negligible, but for comparison with experimental values they should be reduced, since (i) a fraction corresponds to elastically scattered ^{11}Li particles, (ii) the large transverse momenta of ^{9}Li precisely obtained through the scattering process to a large extent are experimentally excluded due to limitations in the large angle acceptance, (iii) the shadowing by the core is probably larger than the shadowing by a neutron corresponding perhaps rather to $r_{nc}=5$ fm and $r_{nn}=4$. Furthermore, the calculations rely on rather uncertain optical model parameters. The effect is almost entirely confined to the absolute values while the shapes of the distributions only are marginally influenced. Using the complete factorization approximation we estimate the size of this cross section to be about 60% of the values of σ^{CD}_{-2n} in Table II. If necessary it can be added at the appropriate places, but we shall in the remaining part of this paper not include this process unless explicitly mentioned.

The radial *neutron momentum distribution after neutron removal* in fragmentation of a 280 MeV/nucleon ^{11}Li projectile on carbon is measured [10]. The variable is p_r, where $p_r^2=p_x^2+p_y^2$ is expressed in terms of the projections p_x and p_y of the neutron momentum along the two directions perpendicular to the beam direction chosen as the z axis. In Fig. 3 we compare our calculations (suitably scaled) for different potentials with the measured momentum distributions in arbitrary units. Without shadowing, shown in part (a), potentials I and III give too broad and too narrow distributions, respectively, whereas potential II with 30% p-wave content reproduces the data. This result is consistent with previous computations without shadowing and diffraction [21,22]. With shadowing, shown in parts (b) and (c), we obtain as expected narrower distributions. Variation from $r_{nc}=3.5$ fm to 4 fm is hardly visible showing a very weak dependence on the r_{nc} shadowing parameter. Now potential III gives a too narrow neutron momentum distributions while potentials I and II both reproduce the data.

The *invariant mass spectrum* of ^{10}Li is independent of the coordinate system and in the rest system of ^{10}Li the invariant mass is (after subtraction of the rest masses) equal to the total kinetic energy E_{nc} of the neutron-^{9}Li system [14,34]. In

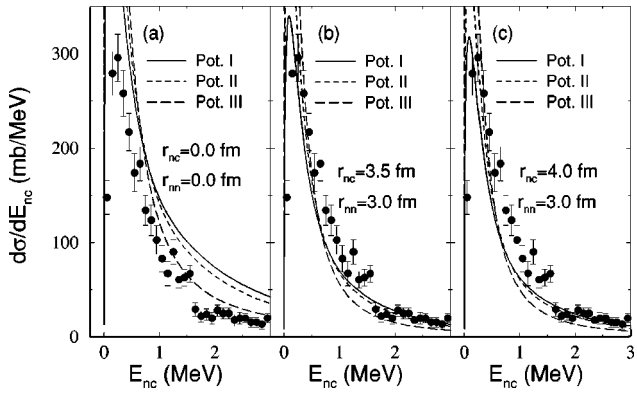

FIG. 4. Invariant mass spectrum of ^{10}Li after fragmentation of ^{11}Li on a carbon target at 280 MeV/nucleon. Only neutron and core spectators forming ^{10}Li are included. The experimental data are from [14]. The calculated curves in (a), (b), and (c) are obtained with the same parameters as in Fig. 2. The maxima for the computed curves in panel (a) (outside the figure) are around 500 mb/MeV, 650 mb/MeV, and 1000 mb/MeV for potentials I, II, and III, respectively. In panels (b) and (c) the maxima for potential II are 430 mb/MeV and 400 mb/MeV, respectively. For potential III we obtain instead 650 mb/MeV and 600 mb/MeV.

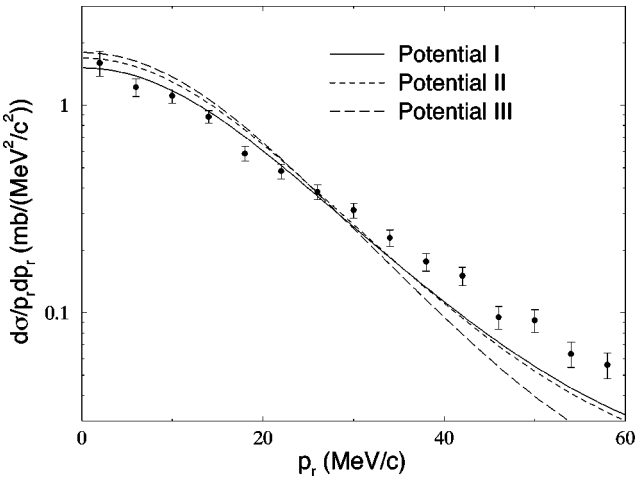

FIG. 5. Radial neutron momentum distribution after core breakup fragmentation of ^{11}Li on a carbon target at 280 MeV/nucleon. The calculations are for the interactions in Table I and a neutron-core shadowing parameter of 4 fm. The ^{9}Li-carbon interaction providing the absolute values is the optical model from [48,49]. The experimental data [11] in arbitrary units are scaled to match the calculations.

Fig. 4 we compare calculations with experimental data obtained after fragmentation of ^{11}Li [14]. The experimental distribution is given in absolute numbers and we compare directly without any arbitrary scaling. We only include processes where the spectators form the detected ^{10}Li, i.e., we neglect those neutron-core combinations where the neutron or the core have been through the scattering process. The latter contributions are relatively small, i.e., the core diffraction and half of the neutron diffraction cross sections. Furthermore the corresponding contributions from these participants are probably not fully included in the measurement.

The calculations without shadowing in panel (a) produce for all potentials distributions with maxima much higher than observed. With shadowing the maxima are reduced as shown in panels (b) and (c), which again are rather similar, but still potentials II and III both give too high peaks. Clearly the best comparison is obtained for potential I and especially with the shadowing in panel (c). The discrepancies appear as a slightly too low-lying peak energy and a slightly too narrow peak. However, the response function of the detector system is not accounted for and a more accurate comparison would shift the peak towards higher values, decrease the maximum value and broaden the peak [14]. Thus all deficiencies may be improved in this way. In any case the behavior of the invariant mass spectrum is strongly influenced by the properties of the low-lying resonances. For example a narrow *p* resonance would produce a shoulder or a peak in the distribution at the position of the resonance. A broader resonance would only show up as a larger cross section at the corresponding position. Thus a more detailed and more accurate comparison between computed and measured distributions would provide information about the neutron-core resonance structure.

The radial *neutron momentum distribution after core breakup* of ^{11}Li on a carbon target at 280 MeV/nucleon is also known experimentally for collisions where ^{9}Li is destroyed [11]. The neutrons are detected in coincidence with a charged fragment different from ^{9}Li. The contribution of neutrons coming from the core is eliminated in the experiment by subtraction of the corresponding neutron momentum distribution obtained from the measured ^{9}Li-carbon reaction.

This distribution arises only from absorption, i.e., we must compute the cross section in Eq. (15), where the ^{9}Li core is destroyed by the target while the neutrons continue unaffected. For simplicity we assume complete factorization such that the ^{9}Li-carbon interaction only is necessary to provide the absolute scale through the absorption cross section. This is a very good approximation for large beam energies. The momentum distribution is then given by Eq. (14) and therefore computed as described in [22]. The absolute cross section is obtained afterwards by multiplication of the absorption cross section computed with the optical model parameters in [48,49] to be 795 mb for a beam energy of 280 MeV/nucleon.

Both from Table II and Figs. 3 and 4 we found good agreement between theory and experiment with the choice $r_{nc}=4$ fm and $r_{nn}=3$ fm for the shadowing parameters. For core breakup reactions, where only the neutron-core shadowing parameter is relevant, we therefore use $r_{nc}=4$ fm in the computation of the neutron momentum distribution shown in Fig. 5. The agreement between theory and experiment is remarkably good in view of the simplicity of the model, where the interactions between the halo neutrons and all the fragments from the core destruction have been neglected. In contrast to the other observables this reaction produces fragments with approximately the same velocity as the halo neutrons and final state interactions beside that of the two neutrons could be significant. The two spectator neutrons could also be disturbed during such violent reactions.

The larger *p*-wave content arising for potential I gives a broader distribution closer to the data than the potentials II and III. The comparison in Fig. 5 is then also supporting the choice of potential *I* and a neutron-core shadowing parameter of 4 fm in the description of the fragmentation reactions of ^{11}Li on a light target.

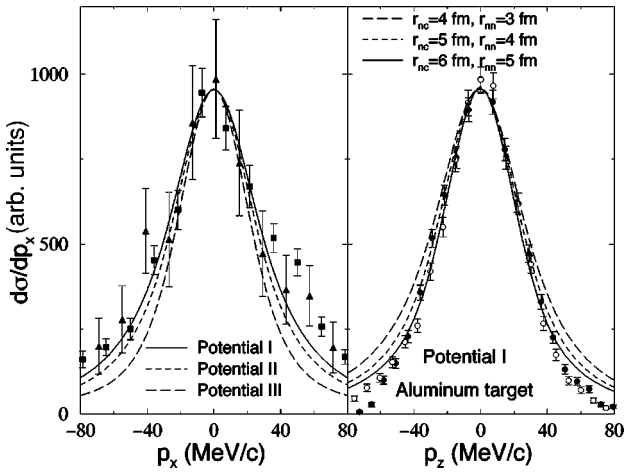

FIG. 6. Momentum distributions for the ^{9}Li core after fragmentation of ^{11}Li. Core diffraction is not included. The left hand side is the transverse distribution for a beam energy of 280 MeV/nucleon on a carbon target and the experimental data is from [12] (filled squares) and [20] (filled triangles). The calculations are for the potentials in Table I with $(r_{nc}, r_{nn}) = (4\ \text{fm}, 3\ \text{fm})$. The right hand side shows the experimental longitudinal distribution for a beam energy of 468 MeV/nucleon (filled circles) and 648 MeV/nucleon (open circles) on an aluminum target [15]. The calculations are for an energy of 280 MeV/nucleon for potential I and the three sets of shadowing parameters specified on the figure. The optical model parameters are from [28]. All the computed distributions are scaled to the experiment.

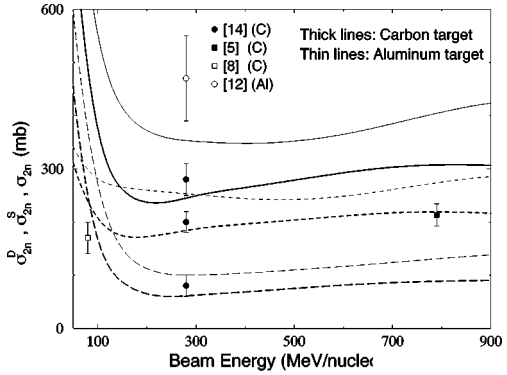

FIG. 7. Two-neutron removal cross sections for ^{11}Li fragmentation on carbon (thick curves) and aluminum (thin curves) as functions of the beam energy. The cross sections from neutron stripping σ^S_{-2n} (short-dashed) and neutron diffraction σ^D_{-2n} (long-dashed) are shown along with the sum σ_{-2n} (solid). The shadowing parameters are $(r_{nc}, r_{nn}) = (4\ \text{fm}, 3\ \text{fm})$ for carbon and $(5\ \text{fm}, 4\ \text{fm})$ for aluminum, the interactions are potential I from Table I and the optical model is specified in [28,49]. The experimental data are from [8,14,5] for increasing energies for carbon and from [12] for aluminum. For [5,8] only the total cross section is given.

The transverse ^{9}Li-*core momentum distribution* for breakup of ^{11}Li on a carbon target at 280 MeV/nucleon is computed and shown in Fig. 6 for the potentials and shadowing parameters in Table I. Detailed comparison with the data [12,15] requires folding of the computed curves with the experimental beam profile resulting in a few MeV broader curves [20]. Due to the large experimental errors this distribution is not very helpful in constraining the potentials and shadowing parameters. However, we can still conclude that the agreement between theory and experiment is satisfactory for potential I.

In Fig. 6 we also show the experimental longitudinal core momentum distribution on an aluminum target for two different beam energies. In the next section we shall show that the difference between longitudinal and transverse momentum distributions is rather small and the widths of the distributions are almost independent of the beam energy. The difference between the transverse and longitudinal data in Fig. 6 can be explained by the use of a different target in the experiments. The aluminum radius is almost one fermi larger than the carbon radius, the optical model parameters are different and more important the shadowing parameters must be larger for aluminum with the resulting narrower momentum distributions as seen in Fig. 6. Still the tail of the distribution is not reproduced. The theoretical prediction of the two-neutron removal cross sections for fragmentation of ^{11}Li on an aluminum target are shown in Table II. The parameters $(r_{nc}, r_{nn}) = (5\ \text{fm}, 4\ \text{fm})$ are consistent with Eq. (28) and the corresponding two-neutron removal cross section is then expected to be $\sigma_{-2n} \approx 350$ mb.

The conclusion of this section is that potential I with the shadowing parameters $(r_{nc}, r_{nn}) = (4\ \text{fm}, 3\ \text{fm})$ for a carbon target gives an excellent agreement between theory and experiment for the observables discussed. This is a strong justification for the model and the method.

IV. BEAM ENERGY DEPENDENCE

We have now established a model with a set of parameters successfully reproducing a variety of experimental data, i.e., potential I, $r_{nc} = 4$ fm, $r_{nn} = 3$ fm and optical model parameters from [28,49]. In the remaining part of this paper we shall only use these parameters and explore the consequences of the model for a number of observables. Particularly we shall in the following concentrate on the predicted energy dependence of various quantities in fragmentation reactions of ^{11}Li on carbon. The model only has a dependence on the beam energy through the interaction between the participant and the target. This interaction is described by phenomenological optical models, which give absorption and elastic scattering cross sections as functions of particle energy, see Fig. 2. These cross sections are decisive factors in Eqs. (12) and (15) and two-neutron removal cross sections must show the same energy dependence.

This is indeed seen in Fig. 7 where we show two-neutron removal cross sections as functions of the beam energy. These calculations do not include two-neutron absorption processes and processes where the core interacts with the target. The cross sections are clearly governed by the behavior of the neutron-carbon cross section, with a minimum at a beam energy of around 250 MeV/nucleon. For larger energies we observe smooth increases towards a flat region. For smaller energies the cross sections increase rather dramatically. The prediction is an increase by about 70% when carbon and aluminum are interchanged as target. The computed curves underestimate the latest experimental points [14], as expected due to the neglect of core diffraction. On the other hand, the older data are far below the calculations. However, at 30 MeV/nucleon total two-neutron removal cross sections are measured for targets of beryllium 0.47 ± 0.10 b and

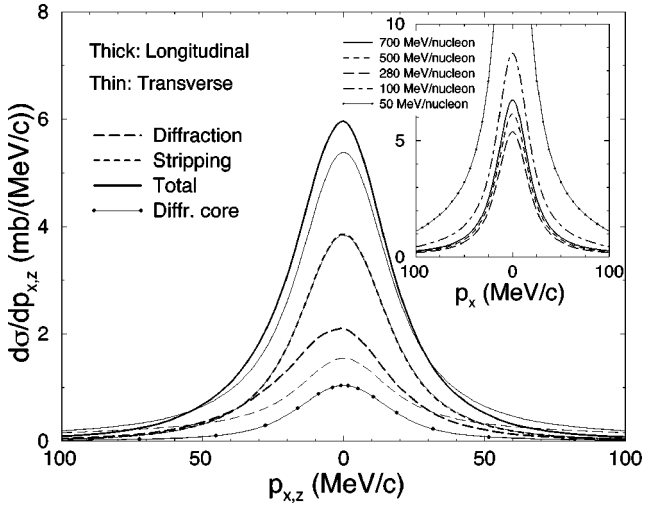

FIG. 8. Longitudinal (thick) and transverse (thin) neutron momentum distributions in coincidence with ^{9}Li after fragmentation of ^{11}Li on carbon at 280 MeV/nucleon computed in the rest frame of the projectile. The beam momentum is the reference direction. The short-dashed and long-dashed curves are the contributions to the total (solid) from diffraction and stripping of the participant neutron. Core diffraction is shown separately as the filled circles. The inset shows the total transverse neutron momentum distribution for the same reaction for different beam energies in the same unit. The standard set of parameters in Fig. 7 is used.

nickel 1.3 ± 0.4 b [7]. This is in agreement with the computed increase towards smaller beam energies.

The two-neutron removal cross sections can be separated into a number of differential cross sections. We shall discuss the momentum distributions of the halo particles both relative to each other and individually with respect to the center of mass of the projectile. In addition we shall discuss the invariant mass of ^{11}Li and the angular correlation of the emitted neutrons. These observables are in most cases not experimentally available and our results are therefore model predictions.

In Fig. 8 we show the neutron momentum distributions after fragmentation of ^{11}Li on carbon. When the participant neutron is absorbed in the stripping process, the detected neutron must be a spectator and then there is no difference between longitudinal and transverse momentum distributions in the rest frame of the projectile. When the participant neutron is scattered by the target (diffraction) it receives additional momentum perpendicular to the direction of the beam. This process therefore contributes with a broader momentum distribution in the transverse than in the longitudinal direction. The tail in the total neutron momentum distribution is then more pronounced for the transverse than for the longitudinal distribution. On the other hand, different tails do not necessarily imply that the full width at half maximum (FWHM) of the distributions also differs. The relative size of the stripping and diffraction contributions reflects the size of the corresponding cross sections in Fig. 7. The contribution to the neutron momentum distribution from the core diffraction (dotted line in the figure) is the same in the longitudinal and transverse directions, as expected because both neutrons are spectators. This contribution of about 30 mb is not added in the figure to the total, but the total width would only be marginally influenced.

TABLE III. The maximum values in mb/(MeV/c) (one-dimensional) and mb/(MeV^2/c^2) (radial) and the FWHM in MeV/c as functions of beam energy in MeV/nucleon for various momentum distributions computed for fragmentation of ^{11}Li on carbon in the rest frame of the projectile. Core diffraction is not included. The subscripts $\perp$, $\parallel$, and r indicate transverse, longitudinal, and radial distributions, respectively. For the radial distributions the FWHM is the width at half maximum multiplied by two. For the invariant mass spectrum we give the maximum value in mb/MeV and the width in MeV.

	Beam energy	50	100	280	500	700
$n_\perp$	max.	18.4	8.7	5.4	6.2	6.7
$n_\perp$	FWHM	42	41	39	39	39
$n_\parallel$	max.	21.6	10.2	6.0	7.1	7.9
$n_\parallel$	FWHM	42	41	39	39	39
$(n$-$^9\mathrm{Li})_\perp$	max.	16.2	8.0	5.2	5.9	6.4
$=(n$-$^9\mathrm{Li})_\parallel$	FWHM	37	37	37	37	37
n_r	max.	2.7	1.3	0.9	1.0	1.1
$\approx(n$-$^9\mathrm{Li})_r$	FWHM	31	31	31	31	31
$(^9\mathrm{Li})_\perp$	max.	9.4	4.5	2.9	3.4	3.7
$=(^9\mathrm{Li})_\parallel$	FWHM	63	63	63	63	63
$(^{10}\mathrm{Li})_\perp$	max.	12.3	6.0	3.9	4.5	4.9
$=(^{10}\mathrm{Li})_\parallel$	FWHM	49	49	49	49	49
inv.	max.	998	488	317	361	394
mass	FWHM	0.42	0.42	0.42	0.42	0.42

The inset in Fig. 8 shows the transverse neutron momentum distribution for different beam energies. The shape of the distributions is essentially independent of the energy due to the approximate factorization in Eqs. (12) and (15) at these fairly high energies, see Table III. The computed FWHM decreases slightly with an energy increase from 50 MeV/nucleon to 280 MeV/nucleon and remains then essentially constant at higher energies. In contrast, the maximum or peak value for the momentum distributions changes considerably with the beam energy. The behavior of the peak values, i.e., a sharp decrease, the passing of a minimum around 250 MeV/nucleon followed by a smooth increase is as expected similar to the variation shown in Fig. 2.

Instead of referring the neutron momentum distribution to the rest system of the projectile as in Fig. 8, we could refer it to the rest system of the spectator neutron-^{9}Li system. Actually in this frame the neutron momentum is the relative neutron-^{9}Li momentum. This momentum distribution is shown in Fig. 9, and it is identical to those of Fig. 8 for an infinitely heavy core. In Fig. 9 we only include the dominating term arising from the spectator neutron and the longitudinal and transverse distributions are therefore identical. The neglected contribution is about half of the diffraction part. The FWHM and the peak values for the curves in the inset are given in Table III. The FWHM is 37 MeV/c for all the energies coinciding with the energy independent width of the stripping part in Fig. 8.

For comparison the neutron-neutron relative momentum

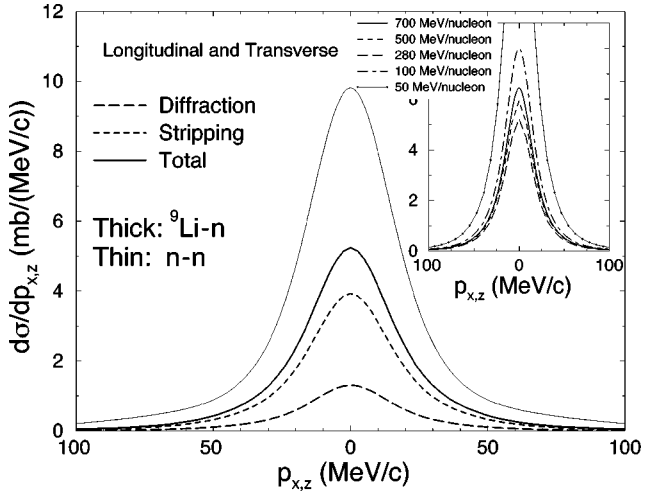

FIG. 9. The neutron-^{9}Li relative momentum distribution for the cases in Fig. 8. The relatively small contributions from the neutron and core participants are not included and the longitudinal and transverse momentum distributions are therefore identical. The neutron-neutron relative momentum distribution computed for core destruction using the complete factorization approximation is also shown for an energy of 280 MeV/nucleon. The carbon-^{9}Li absorption and diffraction cross sections are 795 mb and 419 mb, respectively.

distribution computed using the complete factorization approximation is also shown in Fig. 9. The shape is in this approximation energy independent and the scale is determined by the carbon-^{9}Li absorption (core destruction) cross section. For diffraction (core survival) we should multiply it by about a factor 0.53 for a beam energy of 280 MeV/nucleon.

The two-dimensional radial momentum distributions are often used to increase the number of observed events. The variable is then p_r $(p_r^2=p_x^2+p_y^2)$ and integration of this momentum distribution over p_x (or p_y) gives the transverse momentum. The results are shown in Fig. 10 for the cases in Fig. 9. The widths and the peak values for the curves in the inset are given in Table III. We find the same qualitative behavior as for the one-dimensional distributions. This variation as well as the relative size of the stripping and diffraction contributions are again consistent with the result in Fig. 2.

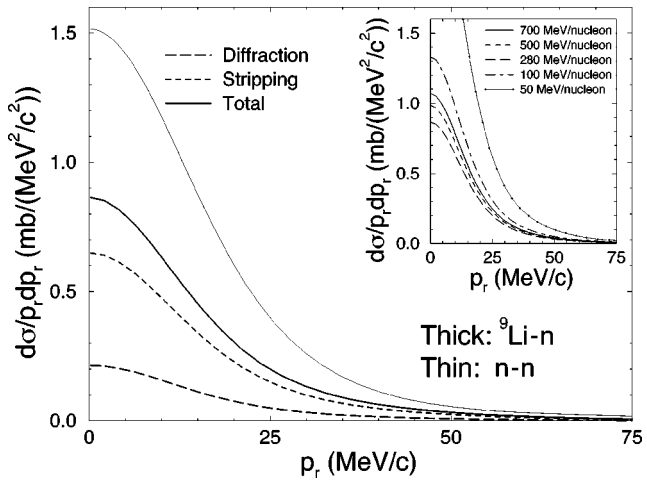

FIG. 10. The radial distributions of the spectator neutron-^{9}Li and the neutron-neutron relative momenta for the cases in Fig. 9.

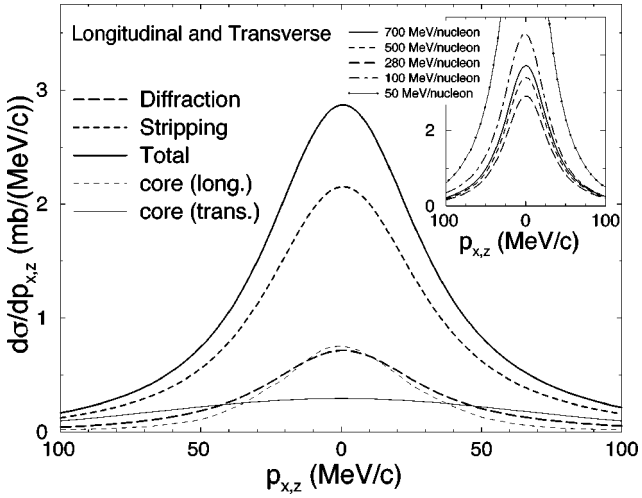

FIG. 11. The ^{9}Li momentum distribution for the cases in Fig. 8. The transverse and longitudinal contributions from the diffracted core are shown separately, but not included in the total cross section. The longitudinal and transverse momentum distributions are therefore identical. The inset shows the distributions in the same unit for different beam energies.

The radial neutron momentum distribution analogous to Fig. 8 is almost indistinguishable from the results in Fig. 10. The cross section for the neutron-neutron momentum distribution corresponds to core destruction for a beam energy of 280 MeV/nucleon. The core survival process is obtained by multiplication with the factor 0.53. The widths are energy independent in this approximation.

The neutron momentum distribution is narrower than that of the ^{9}Li core due to the final state interaction. We show in Fig. 11 the computed ^{9}Li momentum distributions for the same cases as in Fig. 8. The transverse distribution from the diffracted core is small and very broad due to the diffraction process. The longitudinal distribution is as usual narrower. These contributions add about 30 mb to the total cross section while changing only marginally the shape of the total distribution. They are not added in the figure where the total distribution then only includes contributions from the participant neutrons. The displayed longitudinal and transverse momentum distributions are therefore identical, since the difference between them is due to the diffraction process. The inset shows the core momentum distributions for different beam energies. The computed widths and the peak values are given in Table III. The behavior is again a reflection of the results in Fig. 2.

The momentum distributions of ^{9}Li are not far from those found in the simplest approximation described by the Fourier transform of the initial three-body wave function. However, the neutron momentum distributions are strongly influenced by the final state interaction. Instead the momentum distribution of the center of mass of ^{10}Li shown in Fig. 12 reveals direct information about the neutron momentum distribution in the initial three-body system. The process is removal (stripping or diffraction) of one halo neutron by the target with the remaining ^{10}Li system as the two spectators. In the

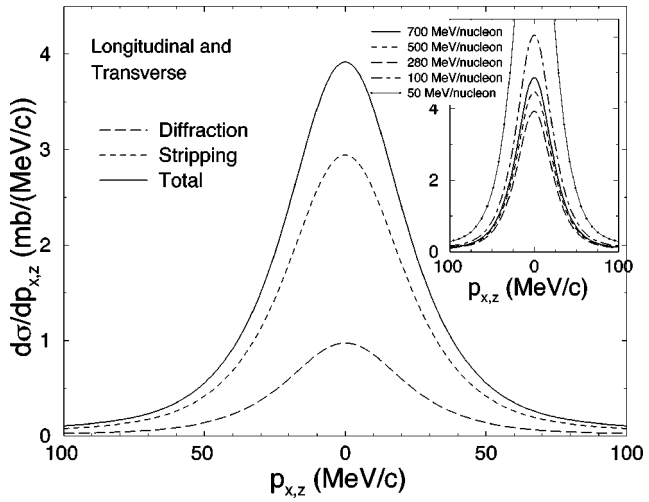

FIG. 12. The momentum distribution for the ^{10}Li center of mass for the cases in Fig. 8. The relatively small contributions from the neutron and core participants are not included and the longitudinal and transverse momentum distributions are therefore identical. The inset shows the distributions in the same unit for different beam energies.

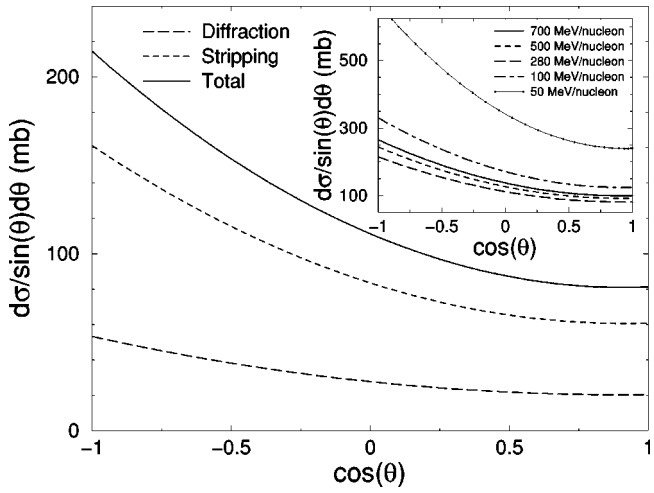

FIG. 13. The distribution of the relative angle θ in the rest frame of the initial three-body system. The angle θ is defined as the angle between the center of mass momentum of ^{10}Li and the relative neutron-^{9}Li momentum. The reactions are the same as in Fig. 8. The relatively small contributions from the neutron and core participants are not included. The inset shows the distributions for different beam energies.

center of mass of the three-body projectile the momentum distributions of ^{10}Li and the participant neutron are then identical.

This observable is insensitive to the final state interaction where the opposite erroneously was postulated in [52]. On the other hand, the sensitivity to the shadowing parameters is large [16,26]. Experimental data could then be very useful to check the validity of the shadowing parameters extracted in the previous section from the comparison between computed momentum distributions and available experimental data. The final state momentum of the participant neutron does not enter in the measured momentum and the longitudinal and transverse ^{10}Li momentum distributions are therefore identical. This can also be understood from the fact that the initial three-body momentum of the participant neutron does not have a preferred direction. The inset of Fig. 12 again shows the variation of the distribution with the beam energy. The behavior is the same as discussed in connection with the previous figures. The related key numbers are given in Table III.

The momentum distributions were recently supplemented by an angular correlation measurement, where the observable is the angular distribution of the relative momentum between the detected neutron and the core in a coordinate system with the z axis along the center of mass momentum of the neutron-plus-core spectator system [17]. This observable is shown in Fig. 13 for our standard case of ^{11}Li fragmentation on carbon. In the computation we assumed that θ is constructed as the angle between the momentum of the center of mass of the ^{10}Li spectator system and the relative momentum between ^{9}Li and the spectator neutron. The small contributions, where the neutron or the core in ^{10}Li are the scattered participants, are not included in this figure, because they are small and furthermore almost completely excluded in the experiment. An estimate of the shape and size of one of the neglected contributions can be found in [27], where both ^{6}He and ^{11}Li fragmentation are discussed.

The computations as always involve Eqs. (12) and (15). The s wave alone produces a constant angular distribution. The p wave alone produces a distribution of the form $1+a\cos^2\theta$, i.e., symmetric around $\cos\theta=0$. For p waves with the projection $m=\pm1$ on the ^{10}Li momentum, a is very small and negative, whereas a for $m=0$ is positive and of the order one. In other words the variation in the angular distribution is almost entirely due to the p wave with projection 0. If both s and p waves are present the distribution takes the form $1+a\cos^2\theta+b\cos\theta$, i.e., becomes asymmetric due to mixing between these partial waves.

Thus our pronounced asymmetry arises from the s and p mixing term, which dominates the angular variation, since the largest contribution from the s wave alone is constant. A dominating p wave would have produced a much more symmetric distribution. Substantial deviations between measured and computed distributions would indicate a selective reaction mechanism emphasizing specific partial waves. The shape of the angular distribution is independent of the beam energy as shown in the inset of Fig. 13. Only the absolute values of the cross section changes in accordance with Fig. 2. The shape in Fig. 13 deviates slightly from that of [27] due to the higher p-wave content.

The momentum distributions reveal properties of the initial three-body system and the reaction mechanism. The invariant mass spectrum of ^{10}Li after fragmentation of ^{11}Li on a light target carry in addition information about the properties of the two-body system. The computed spectrum is shown in Fig. 14, where we only included contributions from the spectator neutron, i.e., the invariant mass E_{nc} is constructed with the momentum of the spectator neutron even when the participant neutron is scattered by the target. In the center of mass system of ^{10}Li the invariant mass is, apart from the rest mass, simply the total kinetic energy of the two-body system.

The spectrum must start from zero due to the phase space. The very low-lying peak is a signature of a dominating

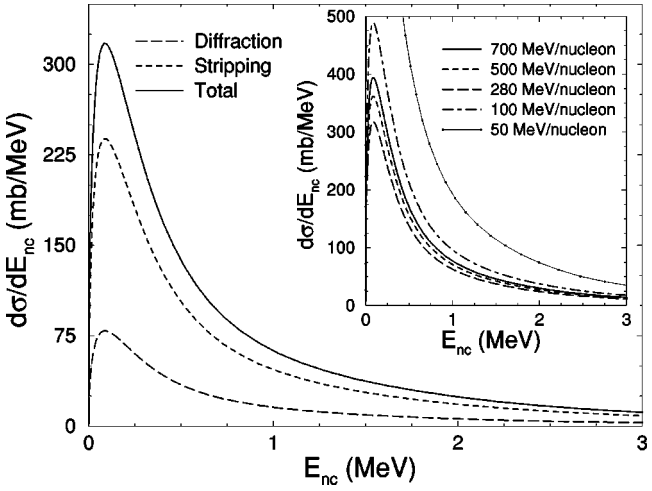

FIG. 14. The invariant mass spectrum of ^{10}Li for the cases in Fig. 8. The rest mass is subtracted. The relatively small contributions from neutron and core participants are not included. The inset shows the distributions for different beam energies.

s-wave contribution. The height of the peak, not the position, reflects the energy of the underlying two-body virtual *s* state. In contrast, a dominating *p*-wave contribution produces a peak at the energy of the corresponding two-body resonance. In the present case the *p*-wave contribution is smeared out in a region around 0.5 MeV. A narrow *p*-wave resonance would show up as a peak in this invariant mass spectrum [22]. The measured spectrum then indicates a low-lying *s* state and a higher-lying *p* resonance with a moderate width, see Fig. 4(c), where the curve computed with potential I is the same as shown in Fig. 14 for a beam energy of 280 MeV/nucleon. The contributions from stripping and diffraction as well as the energy dependence shown in the inset is consistent with the results in Fig. 2. The energy dependence of the peak heights and the widths are given in Table III.

As seen in Table III all the cross sections first decrease with energy and then after a minimum slowly increase again. When the contribution from the scattered neutron is included the widths follow qualitatively the same pattern, although much less pronounced, and in particular they essentially do not vary for energies above around 200 MeV/nucleon. When only the spectator neutron contributes the widths are energy independent. This behavior disagrees with that of [20], but is on the other hand consistent with the experimental results described in [13,15].

In this comparison we implied that our FWHM is the same quantity as the width (or Γ values) discussed in previous experimental papers. Although these quantities are strongly correlated this is not strictly true, since the FWHM precisely is defined as the full width at half maximum of the computed distribution whereas the experimental width is obtained as the width parameter in a fitted function. This easily shifts the emphasis from the small momenta in the calculations to the large momenta of the tail in the experimental analysis. This could easily produce uncertainties of several MeV in the FWHM.

As we have demonstrated the distributions are more complicated than simple one-parameter functions. Comparison of our FWHM with published experimental widths could then be rather misleading. The only safe procedure is to compare directly with the experimental data as we did throughout this paper. On the other hand, then we immediately face the problem that the data too often include purely experimental effects related to beam profile, acceptance range, resolution and target thickness. It is therefore important to compare with the properly interpreted data or alternatively to fold the experimental effects with the calculated results.

V. DISCUSSION AND CONCLUSIONS

Fragmentation reactions of weakly bound two-neutron halo nuclei provide detailed information about structure and reaction mechanism of corresponding three-body systems. The three-body structure can be computed to the needed accuracy provided the interactions are specified whereas the reactions are much more difficult to treat propertly. Our aim is to understand and describe the principal features of all fragmentation observables qualitatively and quantitatively to an accuracy comparable with that of the experimental data. As an important step we have chosen to investigate ^{11}Li considered as a three-body system in a physically simple and transparent model based on geometric properties and phenomenological interactions.

One main assumption is often the sudden approximation where the reaction is instantaneous. The reaction time must then be short compared to the intrinsic time scale of the relative motion of both the three halo particles and the nucleons in the target and the core. Thus the intrinsic motion must be frozen during the collision or equivalently the beam energy must be large compared to the three-body binding energy and the Fermi energy of the target and the core. As expected this approximation has successfully passed the tests at high energies.

In the present model we do not directly use the sudden approximation. We fully include the interaction between the target and each of the halo particles by use of a phenomenological optical model. The description of the interactions is then only limited by the validity range of the parameters employed in the optical model. On the other hand then only elastic scattering is described in details while all other processes are included as absorption from the elastic channel. Fortunately this is precisely the level of information required in discussions of fragmentation reactions, because the inelastic channels overwhelmingly produce different reaction products or particles scattered outside the detection range in the forward direction.

Furthermore we only include the interaction between one halo particle (participant) and the target while neglecting the interactions between the other two halo particles (spectators) and the target. In addition we also neglect the interactions between the spectators and the participant-target system in the final state. The halo particles must then interact independently with the target as three spatially correlated but noninteracting clusters of nucleons. The motion of the spectators must remain undisturbed by the participant-target interaction. More precisely the two criteria for the validity of the model are that (i) the sum of the participant and target radii is less than the halo radius and (ii) the intrinsic velocity of the partipant within the halo is much smaller than the velocity of the projectile or perhaps better that the characteristic time for the intrinsic halo motion is much larger than the collision time.

These main approximations are justified for weakly bound and spatially extended halos colliding with a target with an energy per nucleon larger than the intrinsic kinetic energy of the participant within the halo, i.e., roughly the usual Fermi energy for nuclei although in principle unrelated to the Fermi energies of the nucleons within target and core. With these approximations one halo particle can interact with the target without disturbing the motion of the other two. The total cross section is obtained by adding the contributions from the three possible participants. The sudden approximation is reached when the optical model is reduced to a black sphere when the elastic scattering also is neglected.

The model is described for point particles and the necessary generalization to finite radii involves the concept of shadowing. We eliminate the geometric configurations in the three-body wave function where the spectators move in the shadow of the participant. The need for this correction arises from the simplifying choice of treating the participant-target interaction properly while leaving the spectators untouched in their initial state. If the spectators are close to the participant they would be either absorped or similarly scattered. However, these events contribute in the model computations with the probability given in the initial wave function. Consequently we must omit those unwanted configurations. Another improved treatment with better final state wave functions could directly take these effects into account.

To use the model we must specify the interactions and the shadowing parameters. Within the halo projectile we have the neutron-neutron and neutron-core interactions supplemented by the three-body force. They are parametrized as Gaussians to reproduce the ^{11}Li binding energy, give a neutron-^{9}Li $p_{1/2}$ resonance at 0.5 MeV with a width of 0.4 MeV and finally to produce about 40% of p^2 configurations in the ^{11}Li wave function. These requirements are necessary to reproduce various experimental data. The only freedom left for the halo interactions is then the spin-splitting, arising from the two different couplings to the core spin of 3/2, of both the $s_{1/2}$ and $p_{1/2}$ states in the neutron-core system. The related spin-splitting parameters influence neither the above data nor the fragmentation data. Good agreement with the data then indicates approximately correct statistically averaged positions of the s and p states in ^{10}Li, i.e., 0.71 MeV and 0.76 MeV.

The two-body interactions between halo particles and target are described by use of the phenomenological optical model with parameters adjusted to reproduce the corresponding elastic scattering and absorption cross section data. The two shadowing parameters related to the sizes of halo particles and target are determined to reproduce both the absolute two-neutron removal cross section and the momentum distributions after fragmentation.

We compute all momentum distributions related to fragmentation of ^{11}Li on carbon. For the same reactions we also compute the invariant mass of ^{11}Li and the neutron angular distribution, which recently was measured for ^{6}He fragmentation. These observables are in general consistent with the available measurements. When the neutron and core participants are scattered they receive momentum transfer perpendicular to the beam and the transverse momentum distributions are therefore broader than the corresponding longitudinal distributions. This is then a direct effect of the diffraction mechanism.

The distribution for neutrons is relatively narrow due to the final state interaction, which affects the core less. The distribution for the center of mass of the core-plus-neutron spectators is the broadest reflecting the extension of the initial wave function. Increasing the shadowing parameters decrease the widths of the distributions. The invariant mass reveals information about the low-lying continuum structure of the neutron-plus-core system. The large and very low-lying peak is the signature of a low-lying virtual s state while the shoulder indicates a low-lying and fairly broad p resonance. The angular correlation of the emitted neutrons in the neutron-plus-core center of mass system is highly asymmetric revealing that s and p relative neutron-core states roughly are equally populated in ^{11}Li.

The experimental data are available for several energies and targets, but systematic high precision data given as function of energy for one target does not exist at the moment. We can compute absolute values of a number of differential cross sections. However, in this paper we confined ourselves to the energy dependence of three-body observables for fragmentation on a carbon target with one excursion to an aluminum target. The distributions are essentially independent of target, but the absolute differential cross sections increase with target size. The scaling with target size seems to be somewhat larger than the square of the target radius.

The energy dependence for the given carbon target is computed for a ^{11}Li beam of 50 to 900 MeV/nucleon. The widths of the distributions are essentially constant above around 200 MeV/nucleon and slightly increasing towards lower energies. The absolute values follow the participant-target cross sections. For neutrons this means a smooth increase with energy above around 150 MeV/nucleon and a strong increasee towards lower energies. Furthermore diffraction contributes much less than absorption at energies above 200 MeV/nucleon whereas the inverse is true for energies below 50 MeV/nucleon. This has the consequence that the widths of the transverse distributions are broader at low energies due to the domination of diffraction.

These predictions presuppose that the model is valid at the low energies and the energy dependence of the parameters are correctly included. The criteria for validity indicated relative neutron-target energies above around 20 to 30 MeV and perhaps even lower for very pronounced halo systems. The optical model parameters for the neutron-carbon potential are adjusted to scattering data down to these energies, but the shadowing parameters are assumed to be constant. These parameters have a strong influence on the absolute values of the cross sections and a significant, but much less pronounced, influence on the shapes of the distributions. The predicted widths could perhaps be systematically changed by small amounts due to such possible energy dependence.

In conclusion, we computed systematically essentially all observables for the ^{11}Li three-body fragmentation on a carbon target. The same consistent model is used throughout. Most of the computations are in agreement with available measurements. This strongly indicates that the reaction mechanism essentially is correctly described in the model. The predictions are therefore useful as the unit for compari-

son with future experimental data. Detection of discrepancies would then be significant and therefore also very suggestive of necessary improvements like, for eaxmple, different dependencies of some of the parameters. The same consistent model for all observables is crucial at the present level of accuracy and understanding. In this connection it is worth keeping in mind that treating ^{11}Li as a three-body system is an approxomation and the intrinsic structure must be unavoidable at some point in the interpretation.

ACKNOWLEDGMENTS

We thank K. Riisager for continuous discussions and many suggestions.

APPENDIX: SPIN-1/2 SCATTERING ON SPIN ZERO TARGETS

In Eq. (8) we give the transition amplitude for the scattering process between the participant particle i and the target. Assuming that particle i has spin $s_i=1/2$ and the target has spin zero, we can write the transition amplitude as [33]

$$T^{(0i)}_{\Sigma_i,\Sigma_i'}=-\frac{2\pi}{\mu_{0i}}\langle\chi_{s_i\Sigma_i'}|g(\theta)+h(\theta)(\boldsymbol{n}\cdot\boldsymbol{\sigma})|\chi_{s_i\Sigma_i}\rangle, \quad \text{(A1)}$$

where θ is the angle between $\boldsymbol{p}_{0i}$ and $\boldsymbol{p}'_{0i}$, $\boldsymbol{\sigma}$ are the Pauli spin matrices and the functions $g(\theta)$ and $h(\theta)$ are given by Eqs. (18) and (19), respectively. The vector $\boldsymbol{n}$ is defined as

$$\boldsymbol{n}=\frac{\boldsymbol{p}_{0i}\times\boldsymbol{p}'_{0i}}{|\boldsymbol{p}_{0i}\times\boldsymbol{p}'_{0i}|}, \quad \text{(A2)}$$

$$(\boldsymbol{n}\cdot\boldsymbol{\sigma})=(\boldsymbol{n}\cdot\boldsymbol{\sigma})^{\dagger}=\begin{pmatrix} n_z & n_x+in_y \\ n_x-in_y & -n_z \end{pmatrix}, \quad \text{(A3)}$$

which implies that $(\boldsymbol{n}\cdot\boldsymbol{\sigma})^2=1$.

We can then rewrite the key part of Eq. (10) as

$$\begin{aligned}
&\sum_{Ms_{jk}\Sigma_{jk}\Sigma_i'}\left|\sum_{\Sigma_i}T^{(0i)}_{\Sigma_i\Sigma_i'}M^{JM}_{s_{jk}\Sigma_{jk}\Sigma_i}\right|^2\\
&=\frac{(2\pi)^2}{\mu_{0i}^2}\sum_{\Sigma_i'\Sigma_i\Sigma_i''}\langle\chi_{s_i\Sigma_i}|g^*(\theta)+h^*(\theta)(\boldsymbol{n}\cdot\boldsymbol{\sigma})|\chi_{s_i\Sigma_i'}\rangle\langle\chi_{s_i\Sigma_i'}|g(\theta)+h(\theta)(\boldsymbol{n}\cdot\boldsymbol{\sigma})|\chi_{s_i\Sigma_i''}\rangle\sum_{Ms_{jk}\Sigma_{jk}}M^{JM*}_{s_{jk}\Sigma_{jk}\Sigma_i}M^{JM}_{s_{jk}\Sigma_{jk}\Sigma_i''}\\
&=\frac{(2\pi)^2}{\mu_{0i}^2}\sum_{\Sigma_i\Sigma_i''}\langle\chi_{s_i\Sigma_i}||g(\theta)|^2+|h(\theta)|^2+2\mathrm{Re}[g(\theta)h^*(\theta)](\boldsymbol{n}\cdot\boldsymbol{\sigma})|\chi_{s_i\Sigma_i''}\rangle\sum_{Ms_{jk}\Sigma_{jk}}M^{JM*}_{s_{jk}\Sigma_{jk}\Sigma_i}M^{JM}_{s_{jk}\Sigma_{jk}\Sigma_i''}\\
&=\frac{(2\pi)^2}{\mu_{0i}^2}(|g(\theta)|^2+|h(\theta)|^2)\sum_{Ms_{jk}\Sigma_{jm}\Sigma_i}|M^{JM}_{s_{jk}\Sigma_{jk}\Sigma_i}|^2, \quad \text{(A4)}
\end{aligned}$$

where we used that

$$\sum_{\Sigma_i\Sigma_i''}\langle\chi_{s_i\Sigma_i}|(\boldsymbol{n}\cdot\boldsymbol{\sigma})|\chi_{s_i\Sigma_i''}\rangle\sum_{Ms_{jk}\Sigma_{jk}}M^{JM*}_{s_{jk}\Sigma_{jk}\Sigma_i}M^{JM}_{s_{jk}\Sigma_{jk}\Sigma_i''}=0 \quad \text{(A5)}$$

as seen from Eq. (A3) and the fact that the matrix

$$B^J_{\Sigma_i,\Sigma_i'}=\sum_{Ms_{jk}\Sigma_{jk}}M^{JM*}_{s_{jk}\Sigma_{jk}\Sigma_i}M^{JM}_{s_{jk}\Sigma_{jk}\Sigma_i'} \quad \text{(A6)}$$

is diagonal with identical diagonal elements [22]. Insertion of Eq. (A4) into Eq. (10) and use of Eqs. (11), (14), and (16) then immediately leads to Eqs. (12) and (13).

[1] P.G. Hansen, A.S. Jensen, and B. Jonson, Annu. Rev. Nucl. Part. Sci. **45**, 591 (1995).
[2] B. Jonson and K. Riisager, Philos. Trans. R. Soc. London, Ser. A **356**, 2063 (1998).
[3] M.V. Zhukov, B.V. Danilin, D.V. Fedorov, J.M. Bang, I.J. Thompson, and J.S. Vaagen, Phys. Rep. **231**, 151 (1993).
[4] D.V. Fedorov, A.S. Jensen, and K. Riisager, Phys. Rev. C **49**, 201 (1994).
[5] T. Kobayashi, O. Yamakawa, K. Omata, K. Sugimoto, T. Shimoda, N. Takahashi, and I. Tanihata, Phys. Rev. Lett. **60**, 2599 (1988).
[6] R. Anne *et al.*, Phys. Lett. B **250**, 19 (1990).
[7] K. Riisager *et al.* Nucl. Phys. **A540**, 365 (1992).
[8] B. Blank *et al.* Nucl. Phys. **A555**, 408 (1993).
[9] N.A. Orr *et al.*, Phys. Rev. C **51**, 3116 (1995).
[10] M. Zinser *et al.*, Phys. Rev. Lett. **75**, 1719 (1995).
[11] T. Nilsson *et al.*, Europhys. Lett. **30**, 19 (1995).
[12] F. Humbert *et al.*, Phys. Lett. B **347**, 198 (1995).

[13] N.A. Orr *et al.*, Nucl. Phys. **A616**, 155c (1997).
[14] M. Zinser *et al.*, Nucl. Phys. **A619**, 151 (1997).
[15] H. Geissel, Habilitation, GSI Report GSI-97-03 (1997); H. Geissel and W. Schwab (private communication).
[16] D. Aleksandrov *et al.*, Nucl. Phys. **A633**, 234 (1998).
[17] L.V. Chulkov *et al.*, Phys. Rev. Lett. **79**, 201 (1997).
[18] M.V. Zhukov, L.V. Chulkov, D.V. Fedorov, B.V. Danilin, J.M. Bang, J.S. Vaagen, and I.J. Thompson, J. Phys. G **20**, 201 (1994).
[19] A.A. Korsheninnikov and T. Kobayashi, Nucl. Phys. **A567**, 97 (1994).
[20] M.V. Zhukov and B. Jonson, Nucl. Phys. **A589**, 1 (1995).
[21] E. Garrido, D.V. Fedorov, and A.S. Jensen, Phys. Rev. C **53**, 3159 (1996).
[22] E. Garrido, D.V. Fedorov, and A.S. Jensen, Phys. Rev. C **55**, 1327 (1997).
[23] Y. Ogawa, K. Yabana, and Y. Suzuki, Nucl. Phys. **A543**, 722 (1992); Y. Ogawa, Y. Suzuki, and K. Yabana, *ibid.* **A571**, 784 (1994).
[24] G.F. Bertsch, K. Hencken, and H. Esbensen, Phys. Rev. C **57**, 1366 (1998).
[25] F. Barranco, E. Vigezzi, and R.A. Broglia, Phys. Lett. B **319**, 387 (1993).
[26] E. Garrido, D.V. Fedorov, and A.S. Jensen, Europhys. Lett. **43**, 386 (1998).
[27] E. Garrido, D.V. Fedorov, and A.S. Jensen, Phys. Rev. C **58**, R2654 (1998).
[28] E.D. Cooper, S. Hama, B.C. Clark, and R.L. Mercer, Phys. Rev. C **47**, 297 (1993).
[29] P.G. Hansen, Phys. Rev. Lett. **77**, 1016 (1996).
[30] H. Esbensen, Phys. Rev. C **53**, 2007 (1996).
[31] K. Hencken, G.F. Bertsch, and H. Esbensen, Phys. Rev. C **54**, 3043 (1996).
[32] J. Bang and C.A. Pearson, Nucl. Phys. **A100**, 1 (1967).
[33] A.G. Sitenko and P.J. Shepherd, *Lectures in Scattering Theory* (Pergamon Press, New York, 1971), pp. 228 and 238.
[34] E. Garrido, D.V. Fedorov, and A.S. Jensen, Nucl. Phys. **A617**, 153 (1997).
[35] N. Vinh Mau and J. Pacheco, Nucl. Phys. **A607**, 163 (1996).
[36] H.G. Bohlen *et al.*, Z. Phys. A **344**, 381 (1993).
[37] R.A. Kryger *et al.*, Phys. Rev. C **47**, R2439 (1993).
[38] B.M. Young *et al.*, Phys. Rev. C **49**, 279 (1994).
[39] S.N. Abramovich, B.Ya Guzhovskij, and L.M. Lazarev, Phys. Part. Nuclei **26**, 423 (1995).
[40] A. Cobis, D.V. Fedorov, and A.S. Jensen, Phys. Lett. B **424**, 1 (1998).
[41] A. Cobis, D.V. Fedorov, and A.S. Jensen, Phys. Rev. C **58**, 1403 (1998).
[42] A. Cobis, D.V. Fedorov, and A.S. Jensen, Phys. Rev. Lett. **79**, 2411 (1997).
[43] D.V. Fedorov, A. Cobis, and A.S. Jensen, Phys. Rev. C **59**, 554 (1999).
[44] J.M. Udías, P. Sarriguren, E. Moya de Guerra, E. Garrido, and J.A. Caballero, Phys. Rev. C **51**, 3246 (1995).
[45] H.S. Sherif, R.I. Sawafta, and E.D. Cooper, Nucl. Phys. **A449**, 709 (1986).
[46] T.J. Devlin, W.W. Johnson, K.G. Vosburgh, and R.E. Mischke, Phys. Rev. C **7**, 248 (1973).
[47] J. Franz, H.P. Grotz, L. Lehmann, E. Rösle, H. Schmitt, and L. Schmitt, Nucl. Phys. **A490**, 667 (1988).
[48] P.J. Karol, Phys. Rev. C **11**, 1203 (1975).
[49] C.A. Bertulani, L.F. Canto, and M.S. Hussein, Phys. Rep. **226**, 281 (1993).
[50] T. A. Lasinski *et al.*, Rev. Mod. Phys. **45**, S1 (1973).
[51] J.C. Peng, R.M. DeVries, and N.J. DiGiacomo, Phys. Lett. **98B**, 244 (1981).
[52] T. Aumann, L.V. Chulkov, V.N. Pribora, and M.H. Smedberg, Nucl. Phys. **A640**, 24 (1998).